Neurobiology of Aging 161 (2026) 47–63

Contents lists available at ScienceDirect

Neurobiology of Aging

journal homepage: www.elsevier.com/locate/neuaging.org

Human in vitro and rodent in vivo models highlight progressive mitochondrial dysfunction as a starting point of cerebral amyloidosis

Zahra Motamed [a,b,1,2], Gisela Novack [c,1,3], Daniel Heutschi [a,4], Carine Gaiser [a,5], Corina Garcia [c], Sonia Do Carmo [d,6], A. Claudio Cuello [d], Laura Morelli [c,7], Laura Suter-Dick [a,e,*,8]

[a] University of Applied Sciences and Arts Northwestern Switzerland, School of Life Sciences (FHNW), Muttenz, Switzerland
[b] University of Basel, Basel, Switzerland
[c] Laboratory of Brain Aging and Neurodegeneration, Fundación Instituto Leloir, IIBBA-CONICET, Buenos Aires, Argentina
[d] Department of Pharmacology and Therapeutics, McGill University, Montreal, QC, Canada
[e] Swiss Centre for Applied Human Toxicology (SCAHT), Basel, Switzerland

ARTICLE INFO

Keywords:
Alzheimer's disease
Amyloidosis
Amyloid beta
Mitophagy
Mitochondrial impairment
APP mutations

ABSTRACT

Mitochondrial dysfunction is a well-established hallmark of Alzheimer's disease (AD), particularly in the context of amyloid-beta (Aβ) accumulation. Here, we explored the progression of mitochondrial impairment associated with cerebral amyloidosis in human and rodent systems expressing AD-relevant APP mutations. We investigated mitochondrial function, dynamics, and degradation in human neural progenitor cells differentiated for two and six weeks, carrying the APP (Swedish/London) mutations. These analyses were complemented by studies in 3- and 9-month-old McGill-R-Thy1-APP transgenic (Tg) rats expressing the APP (Swedish/Indiana) mutations. We observed a consistent accumulation of pathogenic Aβ species associated with mitochondrial damage. *In vitro*, early indicators of oxidative stress and initial alterations in mitochondrial network dynamics were evident, including increased mitochondrial reactive oxygen species and elevated total DRP1 levels. Later, after 6 weeks of differentiation, significant mitochondrial dysfunction emerged, including reduced membrane potential, increased mitochondrial network fragmentation, and decreased GSH/GSSG ratio. Mitophagy was also disrupted, as evidenced by reduced localization of TOMM20 to the lysosomes, suggesting impaired mitochondrial clearance. Similarly, hippocampal mitochondria fraction of 9-month-old Tg rats showed elevated fission markers, nitrosative stress, and mitochondrial p62 accumulation, which were absent in 3-month-old Tg animals. Hence, we identified both early and late molecular alterations in mitochondrial homeostasis revealing accumulation of mitochondrial stress, altered dynamics, and mitophagy failure in response to sustained Aβ release. Our results underscore mitochondrial vulnerability during early amyloidosis, identifying it as a potential therapeutic target at initial disease stages. It also reinforces the utility of in vitro models for studying cerebral amyloid pathologies.

1. Introduction

Alzheimer's disease (AD) is a progressive neurodegenerative disorder that presents clinically with memory loss and cognitive decline and is pathologically defined by synaptic loss and the accumulation of extracellular amyloid-β (Aβ) plaques and intracellular neurofibrillary tau tangles (Safiri et al., 2024). Mitochondrial dysfunction has been described among the various factors contributing to AD neuropathology

* Corresponding author at: University of Applied Sciences and Arts Northwestern Switzerland, School of Life Sciences (FHNW), Muttenz, Switzerland.
E-mail address: laura.suterdick@fhnw.ch (L. Suter-Dick).
[1] These authors contributed equally to the work
[2] 0000–0002-0538–2170
[3] 0000–0003-0574–292X
[4] 0009–0008-3295–3355
[5] 0000–0003-4624–461X
[6] 0000–0002-6152–8613
[7] 0000–0001-5159–9015
[8] 0000–0002-1449–3913

https://doi.org/10.1016/j.neurobiolaging.2026.01.006
Received 26 September 2025; Received in revised form 13 January 2026; Accepted 25 January 2026
Available online 27 January 2026

(Hauptmann et al., 2009; W. Wang et al., 2020). Mitochondria support ATP synthesis, regulation of reactive oxygen species (ROS), lipid metabolism, and calcium homeostasis, and the brain's high energy demand underscores its dependence on efficient mitochondrial function (Song et al., 2024).

Familial Alzheimer's disease (FAD) is caused by autosomal-dominant mutations in the *APP*, *PSEN1*, or *PSEN2* genes. These mutations increase production of the toxic Aβ42 isoform, raising the Aβ42/Aβ40 ratio and triggering early-onset pathology (Zhang et al., 2023). Evidence suggests that Aβ, in its soluble, oligomeric, and deposited forms, can directly contribute to mitochondrial damage (Caspersen et al., 2005; Wang et al., 2008). It has been shown that Aβ accumulation reduces mitochondrial mass in both 6-month-old APP/PSEN1 transgenic mice and SH-SY5Y neuroblastoma cells. This effect was reversed by the PDE7 inhibitor S14, which restored biogenesis and limited excessive mitophagy (Bartolome et al., 2018). Evidence supports a mechanistic link between Aβ and mitochondrial damage: Aβ can be imported into mitochondria via the translocase of the outer membrane (TOM) complex and localize to mitochondrial cristae (Hansson Petersen et al., 2008). In addition, accumulation of full-length APP at the mitochondrial import machinery (TOM40/TIM23) in human AD brains has been linked to impaired import of cytochrome c oxidase subunits, reduced complex IV activity, and increased hydrogen peroxide levels (Devi et al., 2006). Together, these studies suggest that Aβ interacts directly with mitochondrial structures, triggering a cascade of functional impairments that have been consistently observed in AD patients as well as in animal and cell models of AD.

Findings from patient brain samples, transgenic animal models, and *in vitro* systems support that AD involves impairment in oxidative phosphorylation, redox homeostasis, and mitochondrial structural integrity (Wang et al., 2025). These changes increase susceptibility to oxidative damage and contribute to synaptic dysfunction through impaired neuronal energy metabolism (Pszczołowska et al., 2024). Oxidative and nitrosative stress are therefore central to AD pathogenesis, arising from an imbalance between antioxidant defense and the production of reactive oxygen and nitrogen species (ROS/RNS) (Butterfield and Boyd-Kimball, 2020; Wang et al., 2014). In neurons from AD brain tissue, Hirai et al. demonstrated elevated levels of oxidative stress markers, including 8-hydroxyguanosine and 3-nitrotyrosine, which co-localized with mitochondrial abnormalities, such as altered morphology, abnormal mitochondrial DNA distribution, and reduced mitochondrial number (Hirai et al., 2001). Consistent with early mitochondrial vulnerability, CRND8 mice exhibit mitochondrial fragmentation and abnormal distribution as early as at three months of age, before substantial plaque deposition. These alterations were accompanied by disrupted cristae structure and reduced bioenergetic capacity (Wang et al., 2017). Other studies also show that Aβ deposition and soluble oligomers promote mitochondrial oxidative stress, increasing neuronal mitochondrial ROS. In 12-month-old McGill-R-Thy1-APP transgenic (Tg) rats, elevated levels of 3-nitrotyrosine (3-NT), a marker of nitrosative stress, have been associated with altered mitochondrial Complex I assembly and enhanced nitro-oxidative damage (Novack et al., 2025). Altogether, these findings indicate that oxidative and nitrosative stress are not only markers of mitochondrial dysfunction but also early contributors to AD progression (Calvo-Rodriguez et al., 2024).

In addition to impaired cellular respiration, mitochondrial dysfunction can lead to distorted mitochondrial networks. These networks are maintained by the balance between fission and fusion and are essential for maintaining cellular health. In AD, excessive mitochondrial fission and impaired fusion lead to fragmented mitochondrial networks, reduced ATP production, and neuronal death (Flannery and Trushina, 2019; Kandimalla and Reddy, 2016). Consistent with this, studies in 12-month-old McGill-R-Thy1-APP transgenic (Tg) rats show that cerebral Aβ accumulation alters the fission–fusion balance (Novack et al., 2025). Increased fission of mitochondrial networks is a marker of cellular distress, as non-functional mitochondria are split from the continuous networks and degraded via mitophagy. Furthermore, Aβ and hyperphosphorylated tau further exacerbate mitochondrial dysfunction in AD by interfering with mitochondrial transport and quality control pathways (Manczak et al., 2011).

The selective autophagic removal of damaged mitochondria plays also a vital role in maintaining mitochondrial homeostasis. Emerging evidence indicates that mitophagy is dysregulated in AD brains, contributing to the progressive accumulation of dysfunctional mitochondria and neurodegeneration (Mary et al., 2023). iPSC-derived neural stem cells carrying the PS1 M146L mutation exhibit impaired mitophagy and mitochondrial dysfunction, and pharmacological induction of autophagy with bexarotene restores autophagic flux and alleviates mitochondrial anomalies (Martín-Maestro et al., 2019). In another study by this group, fibroblasts and iPSC-derived neurons from familial AD patients with the PS1 A246E mutation displayed mitophagy failure due to impaired autophagic degradation linked to lysosomal dysfunction, resulting in the accumulation of Parkin-tagged damaged mitochondria, consistent with a block in mitochondrial clearance downstream of Parkin recruitment (Martín-Maestro et al., 2017). In line with the importance of this pathway, Parkin overexpression has been reported to partially rescue mitophagy and reduce Aβ-associated mitochondrial stress in AD-relevant settings (H. Wang et al., 2020).

While mitochondrial dysfunction is a well-established consequence of Aβ accumulation in AD, most experimental models either examine late-stage pathology, where amyloid deposition and neuronal loss are already evident, or acute Aβ exposure in immature cultures, often through exogenous peptide treatment. In our previous work, we demonstrated that treatment of progenitor neural cells exposed to exogenous Aβ42 for 48 h led to internalization of the peptide and was sufficient to induce mitochondrial impairment, evidenced by an increase in ROS and low mitochondrial membrane potential (Motamed et al., 2025). However, this does not fully model the chronic toxicity of Aβ characteristic of AD. To investigate the impact of sustained Aβ production on mitochondrial health, we compared two amyloidosis models expressing pathogenically similar APP mutations: an *in vitro* system using neural progenitor cells (ReN-APP) carrying the Swedish and London mutations (K670N/M671L (Swedish) and V717I (London)), and an *in vivo* rat model expressing the Swedish and Indiana mutations (K670M/N671L (Swedish) and V717F (Indiana)). Previous findings showed extracellular Aβ deposits in ReN-APP cells from 6 weeks of differentiation (Choi et al., 2014) and in transgenic rats aged 6 months and older (Leon et al., 2010).

This study aimed to characterize progressive mitochondrial dysfunction caused by Aβ at different stages. We endeavoured to model early stages of AD, before extracellular Aβ deposits become evident, and later disease stages where Aβ deposition can already be observed. To this end, we assessed mitochondrial function and morphology at 2 and 6 weeks of differentiation (*in vitro* human model), and 3 and 9 months of age (*in vivo* rat model).

Our data reveal a temporal evolution of mitochondrial involvement in the pathology, with minor effects detected at early time points. Subsequently, in later stages of amyloidosis, significant mitochondrial impairment becomes evident, including elevated mitochondrial superoxide levels, reduced membrane potential, and disrupted network morphology. Specifically, mitophagy was markedly impaired at 6 weeks in ReN-APP cells. Also, hippocampi of 9-month-old Tg rats showed increased nitrosative stress and elevated DRP1 expression, indicating excessive mitochondrial fission. These findings are in agreement with previous results using the same Tg rat stain and showing impaired mitochondrial respiration in the hippocampus (Martino Adami et al., 2019, 2017) and altered levels of mitochondrial super complexes (Novack et al., 2025). In addition, our results also show alterations in the mitochondrial degradation pathway, supporting the notion of progressive mitochondrial dysfunction in response to sustained Aβ exposure (Bordi et al., 2016; Hein et al., 2025).

2. Materials and methods

2.1. Generation of neurons and astrocytes from ReN-P neural progenitor cells

The ReN cell VM human neural progenitor cell line (ReN-P) Millipore, #SCC008) was cultured on Matrigel® Basement Membrane Matrix, phenol red-free (Corning, #356237), in T25 flasks. Cells were seeded at a density of 1×10^4 cells/cm^2 and maintained in proliferation medium composed of DMEM/F12 (Gibco, #11320074), supplemented with 2 µg/mL heparin sodium salt (StemCell Technologies, #07980), 2 % B27 (Invitrogen, #17504–044), 20 ng/mL epidermal growth factor (EGF) (Millipore, #GF144), 20 ng/mL Basic fibroblast growth factor (bFGF) (Millipore, #GF003), and 1 % penicillin/streptomycin/amphotericin B (Abcam, #ab287912). Cells were incubated at 37°C with 5 % CO_2 and passaged every 3–4 days upon reaching confluency. To drive ReN-P cells toward both neuronal/glial differentiation, cells were cultured in differentiation medium, consisting of the proliferation medium without EGF and bFGF, with medium changes every 2–3 days.

2.2. Generation of ReN-APP cell lines via lentiviral infection of ReN-P cells

The lentiviral transduction protocol was adapted and modified based on Choi *et al.* (2015) and Motamed et al. (2025). Briefly, a two-round transduction strategy was required to achieve stable GFP expression in ReN-APP cells. Lentiviral particles carrying the pcLV-CMV-MSC polycistronic expression vectors were obtained from SIRION Biotech (Germany). Two constructs were used: one expressing GFP alone (infectious titer: 5.8×10^9 TU/mL), and the other expressing GFP along with full-length APP harbouring FAD mutations K670N/M671L (Swedish) and V717I (London) (infectious titer: 1.75×10^9 TU/mL). ReN-P cells were seeded at a density of 450,000 cells per well in 6-well plates coated with Matrigel®. One day after seeding, cells were pre-treated with LentiBOOST transduction enhancer (SIRION Biotech, Germany) for 30 min before transduction. Cells were then transduced with either the GFP-only vector (ReN-GFP) or the APP-expressing vector (ReN-APP) at a multiplicity of infection (MOI) of 20, followed by spinoculation (90 min at 800 x g). On day three, the transduction medium was removed, and cells were washed three times to stop infection. GFP expression was confirmed on day four by fluorescence microscopy, although the initial transduction efficiency was low. At passage 2 (day 15), cells were re-seeded and re-infected using the same MOI (20), without LentiBOOST but including spinoculation (90 min at 800 x g). The infection was terminated the next day by washing the cells three times. GFP expression was robustly detected at this stage. Cells were subsequently expanded and cryopreserved in ReN Cell Freezing Medium (Millipore, #SCM007).

2.3. FACS enrichment

ReN-P, ReN-GFP, and ReN-APP cell lines were dissociated using Accutase (Millipore, #SCR005). The resulting cell pellets were resuspended in PBS supplemented with 2 % KnockOut™ Serum Replacement (Gibco, #10828010) and 2 % B27 (Gibco, #17504–044) at a concentration 8 x 10^6 cells/mL. Cells were then filtered through 30 µm Celltrics strainers (Partec, #04–004–2326) prior to fluorescence-activated cell sorting (FACS) using a BD FACSAria™ system to enrich for GFP expression. Sorted populations were classified based on GFP intensity into low- and high-expressing groups. Cells were subsequently cultured in proliferation medium, and cryopreserved stocks were generated using ReN cell freezing medium (Millipore, #SCM007).

2.4. Establishment of a thin-layer ReN-APP Cell culture model

To assess mitochondrial function, thin-layer Matrigel® cultures of ReN-P and ReN-APP cells were established as previously described (Choi et al., 2014). Briefly, cold, growth factor-reduced, phenol red-free Matrigel® Basement Membrane Matrix (Millipore, #356231) was mixed with the cell suspension on ice at a 1:2 ratio, then further diluted to a final 1:10 ratio in medium. A total volume of 300 µL of the Matrigel–cell mixture was added to each well of Nunc™ Lab-Tek™ II 8-well chambered glass slides (Thermo Scientific, #154534), with a final seeding density of 3×10^5 cells per well. Cultures were differentiated and maintained for either 2 or 6 weeks, with medium changes every 3 days.

2.5. RT PCR

Total RNA was extracted from ReN-P cells, ReN-APP and ReN-GFP cells using the TRIzol™ reagent extraction protocol. Complementary DNA (cDNA) was synthesized from 1 µg of total RNA using M-MLV reverse transcriptase (Promega, #M1705) and oligo(dT) primers (Qiagen, #79237). Endpoint PCR was performed using gene-specific primers listed in Table 1. The PCR cycling conditions were as follows: initial denaturation at 95 °C for 2 min, followed by 35 cycles of 95 °C for 30 s, 58 °C for 30 s, and 72 °C for 30 s. A final extension step was carried out at 72 °C for 2 min

2.6. Mitochondrial membrane potential measurement

ReN-P and ReN-APP cell lines differentiated for 2 or 6 weeks were washed three times with PBS. To assess mitochondrial membrane potential, cells were incubated with 15 nM tetramethylrhodamine ethyl ester perchlorate (TMRE; Abcam, #ab113852) in culture medium, along with Hoechst 33258 (Thermo Fisher Scientific, #H3569) for nuclear staining. After a one-hour incubation at 37 °C, cells were washed with fresh medium and imaged using confocal microscopy. Cells treated with 15 µM Carbonyl cyanide-p-trifluoromethoxyphenylhydrazone (FCCP) (Abcam, #ab120081) for 1 h were used as a positive control for membrane depolarization. TMRE signal intensity reflects mitochondrial activity. Therefore, total mitochondrial activity per cell was assessed using ImageJ software (version 2.54 f, NIH, USA) by measuring the integrated density (mean intensity times area of the signal) of each image and normalized by nuclear count.

2.7. Mitochondrial ROS measurement

After 2 or 6 weeks of differentiation, ReN cell lines were washed with PBS and incubated with 5 µM MitoSOX™ Red mitochondrial superoxide indicator (Thermo Fisher Scientific, #M36008) prepared in PBS containing Mg^{2+} and Ca^{2+} for 30 min at 37 °C. Nuclei were counterstained with Hoechst 33258 (Thermo Fisher Scientific, #H3569). After incubation, cells were washed with PBS (Mg^{2+}/Ca^{2+}) and imaged live using confocal microscopy. As a positive control, ReN cells were treated with H_2O_2 for 1 h to induce oxidative stress. Image analysis was performed using CellProfiler software (Ver.4.2.1), and total MitoSOX™ fluorescence intensity was quantified and normalized to the number of nuclei per field.

2.8. Immunofluorescence staining

Differentiated ReN cells were fixed with 4 % formaldehyde overnight and were permeabilized and blocked as described in Choi et al. (2014). They were then incubated overnight at 4°C with primary antibodies, described in Table 2. Following primary incubation, the samples were washed three times with TBST containing 0.1 % Tween-20 and then incubated for five hours at room temperature with secondary antibodies diluted as described in Table 2. DAPI (Sigma-Aldrich, #D9542) was used to stain the nuclei. Images were acquired using an Olympus Fluoview FV3000 Confocal Microscope. Live-cell imaging was performed using a 40 × objective, whereas fixed immunostaining images were acquired using a 60 × objective. For each condition and time point, N = 3–5

Table 1
Primer sequences used for RT-qPCR.

Gene	Name	Sequence (5´-3´)	WT[a]-Product length [bp]	MUT[b]-Product length [bp]
APP	APP_SL_FOR1	CTCCTTCCCGTGAATGGAGAG	380	380
	APP_SL_REV2	CCACACCATGATGAATGGATGTG		
APP London	APP_SL_FOR1	See above	-	357
	APP_SL_REV3	CTTCAGCATCACCAAGGTGATCAT		
APP Swedish	APP_SL_FOR1	See above	-	217
	APP_SL_REV1	CATGTCGGAATTCTGCATCCAGA		

[a] WT: Wild type
[b] MUT: Mutant

Table 2
Antibodies used for Immunofluorescence staining.

Protein of interest	Primary antibody	Secondary antibody
β III Tubulin (Tuj-1)	Mouse monoclonal (Sigma, #T8578) /1:500	Goat anti-Mouse IgG Alexa Fluor 647 (Thermo Fisher Scientific, A-21235)/1:400
S100β	Rabbit monoclonal Antibody (Abcam, #ab52642)/1:100	Goat anti-Rabbit IgG Alexafluor 546(Sigma, Taufkirchen, Germany, A-11071)/1:400
TOMM20	Rabbit monoclonal Antibody (Thermo Fisher Scientific, MA5–34964) /1:250	Goat anti-Rabbit IgG Alexafluor 546(Sigma, Taufkirchen, Germany, A-11071)/1:1000
DRP1	Rabbit monoclonal Antibody (Abcam, #ab184247)/ 1:250	Goat anti-Rabbit IgG Alexafluor 546(Sigma, Taufkirchen, Germany, A-11071)/1:1000
PINK1	Rabbit polyclonal Antibody (Novusbio, #BC100–494)/ 1:150	Goat anti-Rabbit IgG Alexafluor 546(Sigma, Taufkirchen, Germany, A-11071)/1:1000
LAMP2	Mouse monoclonal Antibody (Thermo Fisher Scientific, MA1–205)/1:100	Goat anti-Mouse IgG2b Alexa Fluor™ 647 (Thermo Fisher Scientific, A-21242)/1:400

non-overlapping fields were imaged per replicate using identical acquisition settings. Fields of view were selected in a consistent, unbiased manner across the coverslip, avoiding edges and visually compromised regions. Images were analyzed using ImageJ (Schneider et al., 2012), Mitosegnet, and CellProfiller software (Ver.4.2.1). Mitochondrial number was quantified based on TOMM20-positive staining using the published deep-learning pipeline MitoSegNet (Fischer et al., 2020). The TOMM20 channel was segmented to enable precise identification of individual mitochondria. These segmented images were then used to quantify mitochondrial numbers and assess morphometric features, including branch length. Finally, mitochondrial counts were normalized to cell number, determined by DAPI-positive nuclei.

2.9. Glutathione (GSH) measurement in mitochondria

Intracellular glutathione levels serve as a key biomarker of oxidative stress, a condition that can ultimately lead to mitochondrial damage and cell death. To quantify reduced glutathione (GSH) and oxidized glutathione (GSSG), the GSH-Glo™ Glutathione Assay Kit (Promega, #V6911, USA) was utilized. This luminescence-based assay detects GSH by leveraging a chemical reaction in which a luciferin derivative is converted into luciferin in the presence of glutathione.

To determine total glutathione levels (GSH + GSSG), a reducing agent such as Tris-(2-Carboxyethyl) phosphine, Hydrochloride (TCEP) was included to convert GSSG into its GSH, allowing comprehensive analysis of the glutathione redox state. Luminescence was measured using a microplate luminometer (FlexStation 3 microplate reader, Molecular Devices), and values were compared to a GSH standard curve for quantification.

2.10. Quantification of Aβ42 and Aβ40 using a multiplex assay

Aβ40 and Aβ42 levels were quantified using the MSD V-PLEX Aβ Peptide Panel (6E10) Multiplex Assay (Meso Scale Discovery; #K15200E-2). Supernatants were collected from ReN-P and ReN-APP cell cultures after 2 and 6 weeks of differentiation, as well as from *in vivo* rat hippocampal homogenate samples at 3 and 9 months. All samples were diluted 1:2 in Diluent 35 before analysis. The assay was performed according to the manufacturer's instructions. Briefly, non-specific binding sites were blocked with Diluent 35 for 1 h. Following this, SULFO-TAG-conjugated anti-Aβ (6E10) detection antibody, diluted samples, and calibrators were added to the 96-well assay plate and incubated for 2 h at room temperature. After incubation, the plate was washed, read buffer was added, and signal detection was carried out using the MESO QuickPlex SQ 120 instrument (Meso Scale Discovery). According to the Certificate of Analysis for the assay lot used, the lower limit of detection (LLOD) was 9.97 pg/mL for Aβ40 and 0.368 pg/mL for Aβ42. Values from hippocampal homogenates were normalized to protein concentration using the Bradford assay, whereas *in vitro* values were normalized to the number of nuclei.

2.11. Animals and ethical implications

The McGill-R-Thy1-APP transgenic (Tg) rats express the human APP751 transgene with the Swedish and Indiana mutations (Leon et al., 2010). Animals were provided by the Royal Institution for the Advancement of Learning (McGill University-Canada), and an in-house colony was established at the Leloir Institute Foundation (Buenos Aires, Argentina) by cross-breeding Tg with wild-type (WT) Wistar rats. The experimental protocol followed ARRIVE and OLAW-NIH guidelines and was approved by the local Institutional Animal Care & Use Committee (FIL-IACUC N°. 100). Experiments were performed on isolated brains of male rats aged 3-month-old (body weight: 300–340 g) or 9-month-old (body weight: 400–470 g).

Animals were housed in groups of 2–3 in transparent polypropylene cages of standard dimensions (height, 18 cm; width, 33 cm; length, 59 cm; Tecniplast model no. 1354) with *ad libitum* access to water and standard rat chow (Cooperacion, Gilardoni, Buenos Aires, Argentina) under a 12-h light/12-h dark cycle (lights on at 8 a.m.) and controlled temperature and humidity (21°C ± 2°C, 50 % ± 10 %).

Two cohorts, consisting of a total of 8 WT and 8 TG rats, were used for the *in vivo* experiments. Total and mitochondrial fractions were obtained from hippocampal homogenates for further studies. A first cohort (WT = 4; Tg = 4 of 3-month-old animals) was used for the determination of nitrotyrosine-containing proteins, DRP-1 (mitochondrial fission indicator), PINK-1 (a mitophagy marker), p62 (characteristic of early autophagosome formation), and LC3B (a central protein in autophagy) levels. Similar analyses were performed with a second cohort (WT = 4; Tg = 4 of 9-month-old rats). The hippocampal total fraction of both cohorts was used for soluble Aβ measurement.

2.12. Isolation of rat tissue and subcellular fractionation

Animals were anesthetized with an intraperitoneal injection of

ketamine (50 mg/kg) and xylazine (10 mg/kg), perfused intracardially with 0.9 % NaCl/200 U/L heparin, and the brains were quickly removed based on (Leal et al., 2006). For biochemical techniques, hippocampal homogenates were prepared in buffer MSTE w/BSA 1 % (230 mM Mannitol/70 mM Sucrose/10 mM Tris–HCl/1 mM EDTA, pH 7.4) and stored at −80°C until processing (Jha et al., 2016) for the total fraction. Subcellular fractions enriched in mitochondria were obtained from hippocampal homogenates by differential centrifugation following standard procedures (Cadenas and Boveris, 1980). Protein concentration was determined using the Pierce MicroBCA Protein Assay Kit (Thermo Scientific, Cat no. A65453).

2.13. Protein detection by immunoblotting

Protein extracts from total or mitochondrial fractions were separated using SDS-PAGE electrophoresis followed by immunodetection via Western-blot using standard laboratory techniques. Briefly, total and mitochondrial fractions were resuspended in 10 µl MSTE buffer plus 5 µl of sample buffer 4X (0.5 M Tris-HCl pH 6.8; 1 M Dithiothreitol (DTT); 8 % (w/v) Sodium dodecyl sulphate (SDS); 4.3 M glycerol; 6 mM bromophenol blue) followed by a heating-denaturation procedure for 10 min at 100°C. Samples were resolved on 7.5 % Tris-Tricine mini-gels. Proteins were transferred to a PVDF membrane; membranes were incubated with blocking buffer (PBS/5 % skimmed milk) for 1 h at room temperature, followed by three washing steps (10 min each) with PBS/0.1 % Tween 20, before incubations with the primary specific antibodies (overnight at 4°C, Table 3). The next day, the membranes were washed 3 times in PBS/0.1 % Tween, before incubation with the secondary specific antibodies for 1 h at RT (Table 3).

After protein transfer, membranes were incubated with primary antibodies as follows: membranes with mitochondrial or total fractions (one of each) were sequentially incubated with DRP-1, PINK-1, 3-NT, and finally with the appropriate loading control (TOMM20 for mitochondrial fractions, α-Tubulin for total fractions) with stripping (5 min in stripping buffer NaOH 0.1 M) performed between each incubation. Similarly, another set of membranes containing mitochondrial or total fractions were sequentially incubated with p62, LC3, and likewise probed with the corresponding loading controls (TOMM20 or α-Tubulin) with stripping performed between each incubation.

Peroxidase-conjugated secondary antibodies and enhanced chemiluminescence detection system (Amersham ECL Prime Western blotting Detection Reagent, catalogue N° RPN2232) were employed to detect immunoreactivity using Amersham ImageQuant™ 800 biomolecular imager (Cytiva). Quantification of the optical density of the bands of interest was calculated following previous reports(LI-COR, 2018) using Image J software (NIH, USA). Briefly, the normalized band intensity value was calculated by dividing the band intensity of the protein of interest by the band intensity of the corresponding loading control. The ratios were normalized to the band intensity values of the WT samples.

2.14. Immunohistochemistry

Brain tissues were divided into left and right hemispheres. Hippocampus was isolated from left hemisphere and retained for biochemical studies. The right hemisphere was fixed in 4 % paraformaldehyde in 0.1 M phosphate buffer (PB), pH 7.4 overnight at 4°C, and finally transferred to a solution of 30 % sucrose in 0.1 M PB for 5 days, or until sectioned for immunohistochemistry into 40 µm coronal sections with a freezing sledge microtome (SM 2000R, Leica) at −20°C. The sections were blocked by incubating them in normal donkey serum (Sigma, cat no. D9663) 0.1 % in phosphate buffered saline (PBS)-Triton X (0. 05 %) for 1 h at RT, the sections were incubated overnight in a humidity chamber at 4°C with mouse monoclonal anti Aβ (McSA1, Medimabs, catalog N° MM-0015P) at a final dilution of 1:1000 in blocking solution. The next day, sections were washed three times in PBS-Triton X 0.05 %, incubated for 1 h in secondary antibody (Biotin-SP- AffiniPure™ Donkey Anti-Mouse IgG (H+L), Jackson Immuno Research catalogue N° 715–065–151), in PBS at a 1:200 dilution. After the incubation, samples were washed three times in PBS-Tween 0.05 % and incubated for 1 h at RT in VECTASTAIN Elite ABC Kit (catalogue N° PK-6100). After three washes in PBS, the reaction was detected by DAB Substrate Kit (Vector catalogue N° SK-4100) for 2 min and then stopped with double-distilled water. Finally, the sections were dehydrated in ascending graded alcohols, cleared in xylol and finally mounted in synthetic Canada balsam.

2.15. Statistical analysis

Data were analyzed and visualized using GraphPad Prism version 9.3.1 (GraphPad Software). For comparisons between two groups, unpaired Student's *t*-tests were used. If data did not meet assumptions of normality or equal variance, Welch's correction or the Mann–Whitney *U* test was applied as appropriate. For multiple group comparisons, one-way ANOVA was used when assumptions were met; otherwise, the Kruskal–Wallis test was used. $p < 0.05$ was considered significant: (ns) $p > 0.05$; *$p \leq 0.05$; **$p \leq 0.01$; ***$p \leq 0.001$.

3. Results

3.1. ReN-APP cells exhibit functional differentiation and secrete Aβ

To establish a human cellular model for APP-associated pathology, we developed two transgenic ReN cell VM lines: one stably expressing mutant human APP along with GFP (ReN-APP), and a control line expressing only GFP (ReN-GFP) (Fig. 1A). After FACS sorting the transduced cell populations, we proceeded with the GFP-low expressing ReN-APP population, which represented the majority of the transduced

Table 3
Antibodies used for Immunoblotting.

Protein of interest	Primary antibody	Secondary antibody
α-Tubulin	Mouse monoclonal (Developmental Studies Hybridome Bank, # 12G10) /1:2000	Goat anti-Mouse (Jackson, #115–035–146)/ 1:10000
3-nitrotyrosine	Rabbit anti-3NO2Tyr (polyclonal antibody kindly provided by Rafael Radi from the UdeLaR-Montevideo, Uruguay)/ 1:1000	Goat anti-Rabbit (Jackson, #111–035–144)/ 1:10000
TOMM20	Rabbit monoclonal Antibody (Santa Cruz Biotechnology, # SC-114115) /1:1000	Goat anti-Rabbit (Jackson, #111–035–144)/ 1:10000
DRP1	Rabbit monoclonal Antibody (Abcam, #ab184248)/ 1:1000	Goat anti-Rabbit (Jackson, #111–035–144)/ 1:10000
PINK1	Rabbit polyclonal Antibody (Novusbio, #BC100–494)/1:150	Goat anti-Rabbit (Jackson, #111–035–144)/ 1:10000
p62	Rabbit (Cell Signaling, #5114S)/1:1000	Goat anti-Rabbit (Jackson, #111–035–144)/ 1:10000
LC3B	Rabbit (Cell Signaling, #3868S)/1:1000	Goat anti-Rabbit (Jackson, #111–035–144)/ 1:10000

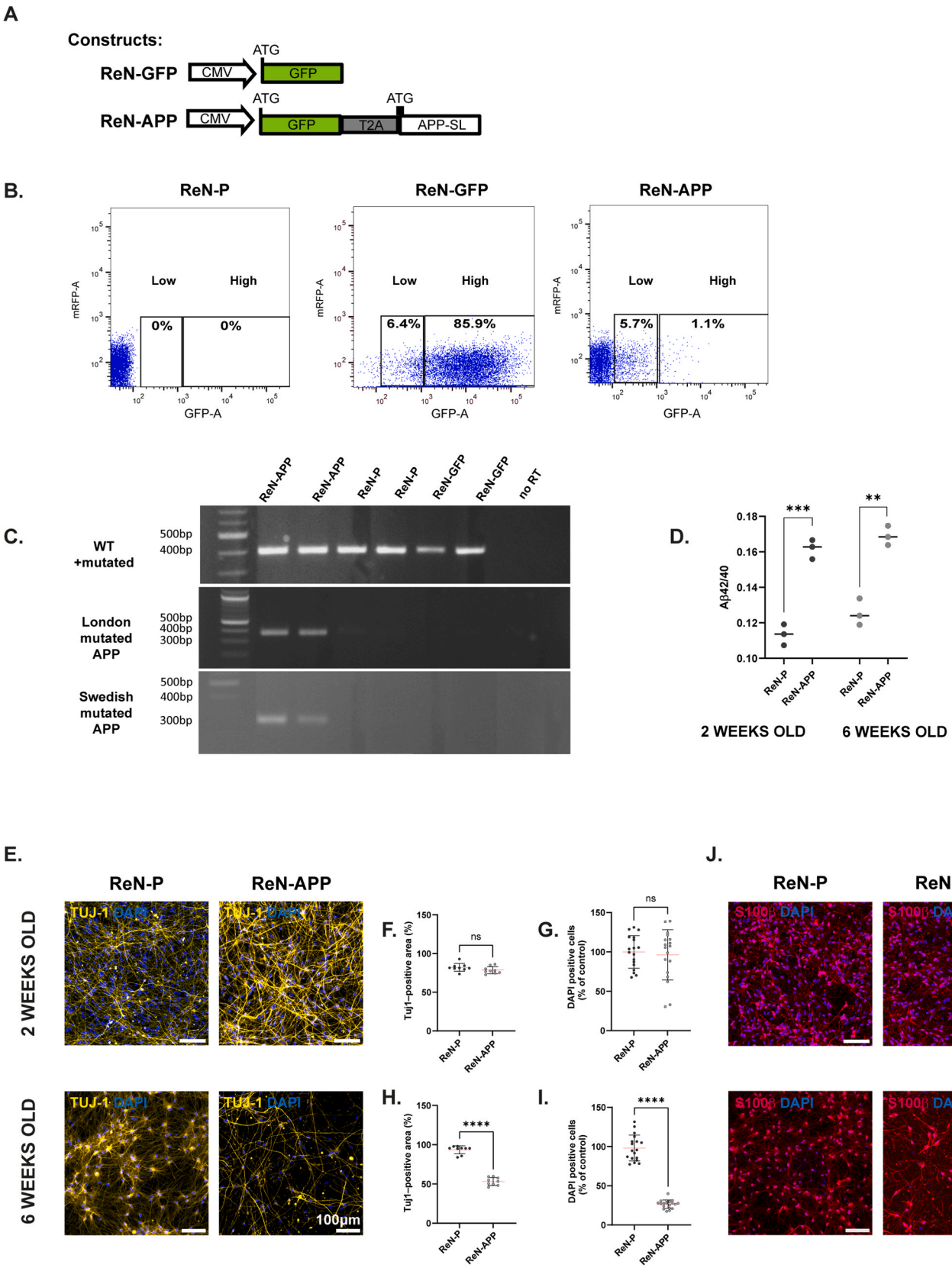

(caption on next page)

Fig. 1. ReN-APP cells exhibit functional differentiation and Aβ Secretion A. Scheme illustrating polycistronic lentiviral constructs used for transduction: one carrying only GFP as a control (ReN-GFP), and another carrying APP with Swedish and London mutations (APP-SL), referred to as ReN-APP. Constructs include IRES (internal ribosome entry sites) and are driven by a CMV (cytomegalovirus) promoter. **B** FACS analysis used to sort cells based on GFP expression, confirming successful transfection. % values indicate number of GFP-positive cells in each gated population (high and low). **C** RT-PCR analysis of gene expression levels in transfected cells. WT = wild-type **D** Quantification of an Aβ42/40 ratio in the supernatant of 2 and 6 weeks. **E, J** Immunofluorescence staining of differentiated cells at 2 and 6 weeks using βIII Tubulin (Tuj1, neuronal marker in yellow) (E), S100β (astrocyte marker, red) (J), and DAPI (nuclear stain, blue) to assess cellular differentiation over time. **F, H** Quantification of Tuj1 staining in 2- and 6-week ReN-P and ReN-APP cultures. Data are expressed as Tuj-1–positive area (% of total image area), $N \geq 3$. **G, I** Quantification of cell density based on DAPI-positive nuclei counts per field in 2- and 6-week cultures. Data are shown as scatter plots with mean ± SD. Normality was assessed using the Shapiro–Wilk test. For comparisons between two groups, normally distributed data with homogenous variances were analyzed using unpaired *t*-tests; when normality or equal variance assumptions were not met, Mann–Whitney tests were used. ns, not significant, $*p < 0.05$; $**p < 0.01$; $***p < 0.001$, $****p < 0.0001$.

cells (Fig. 1B). Stable integration and expression of the transgenes were confirmed by RT-PCR, showing the presence of both APP mutations (London and Swedish) in the ReN-APP cells, but not in the parental control cells (ReN-P) nor the ReN-GFP control line (Fig. 1C). Removal of growth factors from the cell culture medium for one week promoted the differentiation of transduced cells into a mixed population containing neuronal cells and astrocytes (Fig. 1E, J).

At one week, ReN-P and transduced cells acquired expected rounded cell bodies and notable neurite outgrowths shown by brightfield and live GFP images (Supplementary Fig. 1A). Cultures maintained for 2 weeks showed extensive interconnected networks, consistent with more differentiated cells. Differentiation was confirmed by immunofluorescence staining, which revealed expression of the neuronal marker β III Tubulin- (Tuj1) (Fig. 1E) and the astrocytic marker S100β (Fig. 1J). The 6-week timepoint was selected as a final endpoint due to the emergence of phenotype-specific features such as neuronal loss and large astrocytic soma size in the ReN-APP line (Fig. 1E, J). Quantification of Tuj1 staining confirmed these observations. At 2 weeks, the percentage of Tuj1–positive area did not differ between ReN-P and ReN-APP cultures, whereas at 6 weeks, ReN-APP cultures displayed a significant reduction in Tuj1–positive area compared with ReN-P (Fig. 1F, H). Likewise, DAPI-positive nuclei count per field was comparable between the two groups at 2 weeks but was significantly reduced in 6-week ReN-APP cultures (Fig. 1G, I), indicating decreased cell density at the later time point.

To evaluate disease-relevant features of the model, soluble Aβ42 and Aβ40 levels were quantified in the supernatants of 2- and 6-week-old cells cultured in a thin Matrigel® layer. ReN-APP cells showed a significant increase in Aβ42 secretion, approximately ~3-fold at 2 weeks and ~2.4-fold at 6 weeks, compared to ReN-P controls (Supplementary Fig. 1B). In contrast, Aβ40 levels were significantly elevated only at 2 weeks (~2.3-fold) and remained unchanged at 6 weeks (Supplementary Fig. 1C). This measurement resulted in an elevated Aβ42/Aβ40 ratio in ReN-APP cultures compared to controls, with a similar increase of approximately 1.4-fold at 2 weeks and 1.3-fold at 6 weeks, indicative of an amyloidogenic profile. (Fig. 1.D). At this later time point, we also observed a decrease in cell numbers.

Collectively, these findings demonstrate that the ReN-APP cell line reliably expresses mutant APP Swedish/London, maintains its capacity for neural and astrocytic differentiation, and recapitulates key pathological features, including altered Aβ processing. The 2-week differentiation period served as an early time point, at which only minimal morphological changes were observed, whereas the 6-week differentiation period reflected a later stage with more pronounced alterations in neuronal and astrocytic morphology, accompanied by cell loss.

3.2. Early oxidative imbalance and later loss of membrane potential indicate progressive mitochondrial dysfunction

To assess overall mitochondrial functionality in ReN-APP cells during AD pathology, mitochondrial membrane potential (MMP) was measured using tetramethylrhodamine ethyl ester (TMRE) staining at 2 and 6 weeks of differentiation. A significant reduction in TMRE fluorescence per cell was observed in ReN-APP cells after 6 weeks compared to control ReN-P cells (Fig. 2C-D), while no significant difference was detected in 2-week-old ReN-APP cells (Fig. 2A-B), indicating that mitochondrial functionality is still intact at early stages of AD pathology and diminishes over time as the amount of Aβ peptides increases. ReN parental cells treated with FCCP, used as a positive control, showed lower TMRE fluorescence compared with the other two groups at both 2 and 6 weeks (Supplementary Fig. 1D, D)

Mitochondrial ROS production typically precedes the loss of mitochondrial function. Therefore, we assessed mitochondrial superoxide production in ReN-APP cells at 2 and 6 weeks of differentiation using MitoSOX staining. Elevated MitoSOX fluorescence was detected in ReN-APP cells at both time-points, relative to control cells (Fig. 2E-H). When treated with H_2O_2 as a positive control, ReN parental cells showed higher Mitosox signal compared to control group at 2 and 6 weeks (Supplementary Fig.1E, E´). To evaluate redox status, we measured levels of reduced glutathione (GSH) and oxidized glutathione (GSSG) and calculated the ratio. The ratio of GSH/GSSG is often used as a marker of oxidative stress, as it shows the remaining antioxidative capacity inside the cell. While no significant difference in GSH/GSSG ratio was observed at 2 weeks (Fig. 2I), a significant decrease was detected in ReN-APP cells at 6 weeks compared to controls (Fig. 2J), indicating impaired redox balance at later stages of differentiation. Furthermore, this hints that superoxide production is continuously elevated in ReN-APP cells.

3.3. Disrupted mitochondrial dynamics in early and late-stage APP-expressing cell lines

Prolonged oxidative stress has been shown to be further associated with mitochondrial network fragmentation and loss of mitochondria. To investigate mitochondrial dynamics, we performed immunostaining for DRP1, a key mediator of mitochondrial fission. Quantitative analysis of DRP1 signal revealed a significant increase in total DRP1 levels in ReN-APP cells compared to ReN-P controls at both 2 and 6 weeks (Fig. 3A–C). This elevation suggests an early and sustained shift towards enhanced fission capacity in ReN-APP cells, potentially as an adaptive response to accumulating mitochondrial stress.

To assess whether the increased DRP1 expression was indeed associated with morphological changes in mitochondrial networks, we stained cells with TOMM20 (a mitochondrial outer membrane marker) and analysed the mitochondrial network architecture. At 6 weeks, ReN-APP cells exhibited significantly reduced average mitochondrial branch length, indicative of increased mitochondrial fragmentation. In contrast, no differences in branch length were observed at the 2-week stage (Fig. 3D–F). Consistent with this, quantification of mitochondrial number revealed a higher number of mitochondria in 6-week-old ReN-APP cells compared to controls, whereas no difference was observed at 2 weeks. These findings collectively support the occurrence of enhanced mitochondrial fission at the 6-week stage in ReN-APP cells (Fig. 3E- G).

3.4. Impaired mitophagy in the late stage of ReN-APP cells

Following the detection of mitochondrial impairment and fragmentation of the mitochondrial network in ReN-APP cells after 6 weeks of differentiation, we next became interested in evaluating whether

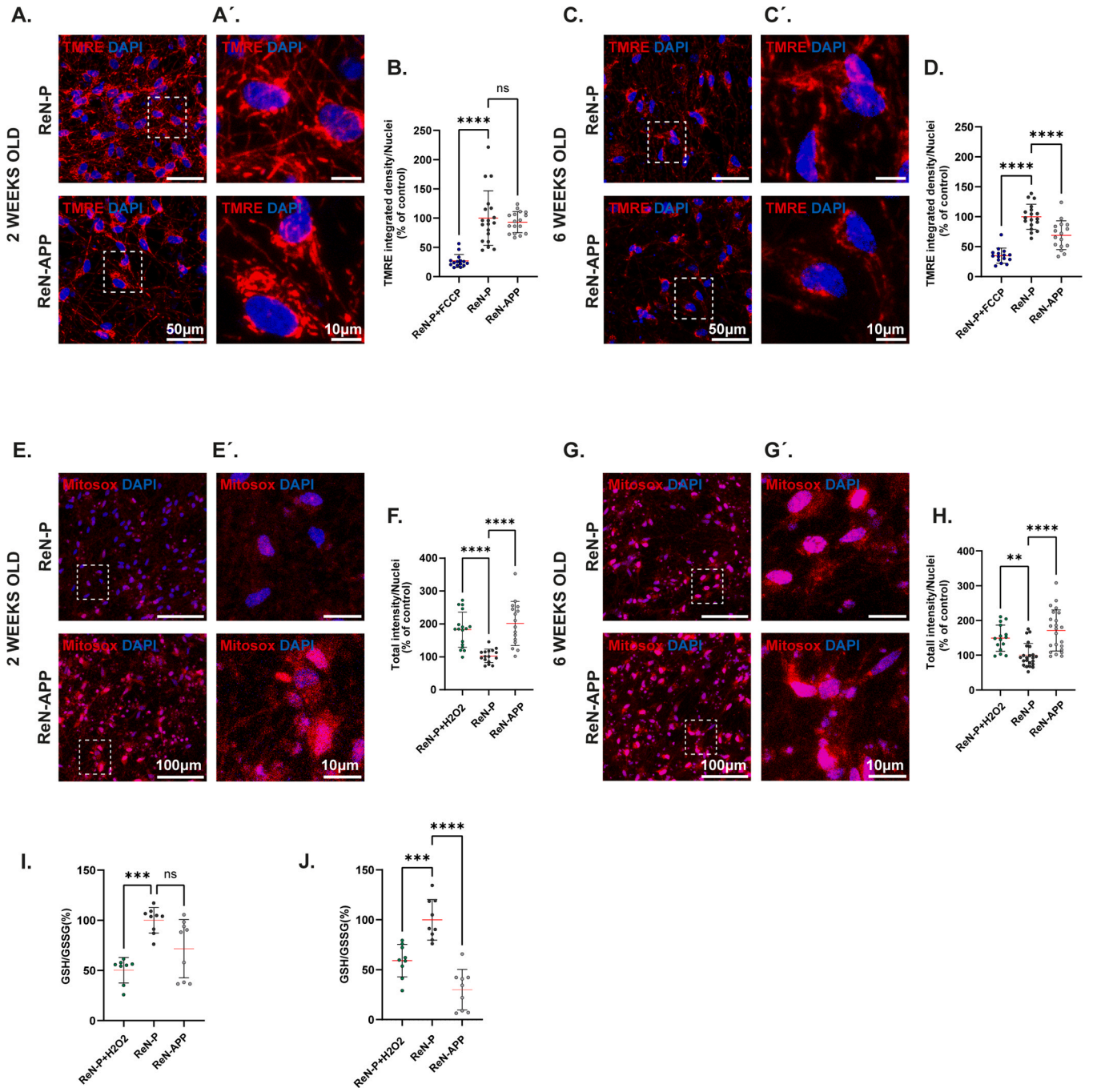

Fig. 2. Early oxidative imbalance and later loss of membrane potential indicate progressive mitochondrial dysfunction A, D. Live cell imaging of 2 and 6-week-differentiated ReN-P and ReN-APP cells using TMRE (red) to assess mitochondrial membrane potential, and Hoechst (blue) for nuclear labelling. Scale bar: 50 µm. Images were acquired using a confocal laser microscope (Olympus FV3000). **B, D**. Mitochondrial activity was analyzed as an integrated density normalized to nuclei using CellProfiler (v4.2.1). **A′, C′:** Zoomed-in views of the boxed regions in A and C, showing TMRE signal (red) in the cells. Scale bar:10 µm. **E, H** 2- and 6-week-old ReN-P and ReN-APP cells stained with MitoSOX™ Red to detect mitochondrial superoxide, and Hoechst (Blue) to label nuclei. Scale bar: 100 µm. **F, H** MitoSOX™ total fluorescence intensity measured using CellProfiller (v4.2.1) for 2 and 6 weeks, respectively. Control values were set to 100 %. H_2O_2-treated cells were included as a positive control. **E′, G′:** Zoomed-in views of the boxed regions in A and C, showing MitoSOX™ fluorescence as a readout of mitochondrial superoxide. Scale bar: 10 µm. **I, J** Quantification of intracellular GSH/GSSG ratio in 2- and 6-week differentiated cells, with H_2O_2 used as a positive control. n = 3 independent biological replicates with N ≥ 5 images per group. Data are shown as scatter plots with mean ± SD. Statistical significance was assessed using one-way ANOVA or Kruskal–Wallis, chosen based on distributional assumptions. ns, not significant, *p < 0.05; **p < 0.01; ***p < 0.001, ****p < 0.0001.

mitophagy is altered. To assess mitophagy initiation, we measured the expression level of PINK1, a key mitophagy initiator, in ReN-APP and ReN-P cells. Data revealed that after 6 weeks, PINK1 levels were significantly elevated in ReN-APP cells compared to controls, whereas no significant differences were observed at the 2-week time point (Fig. 4A-C). This suggests an activation of the mitophagy pathway in response to mitochondrial dysfunction in ReN-APP cells.

Given the significant mitochondrial network fragmentation and elevated mitophagy initiation observed in 6-week-old ReN-APP cells, we next wanted to evaluate whether mitophagy progression was impaired. Specifically, the delivery of mitochondria to lysosomes and the extent of mitochondrial degradation. Therefore, we performed co-staining of

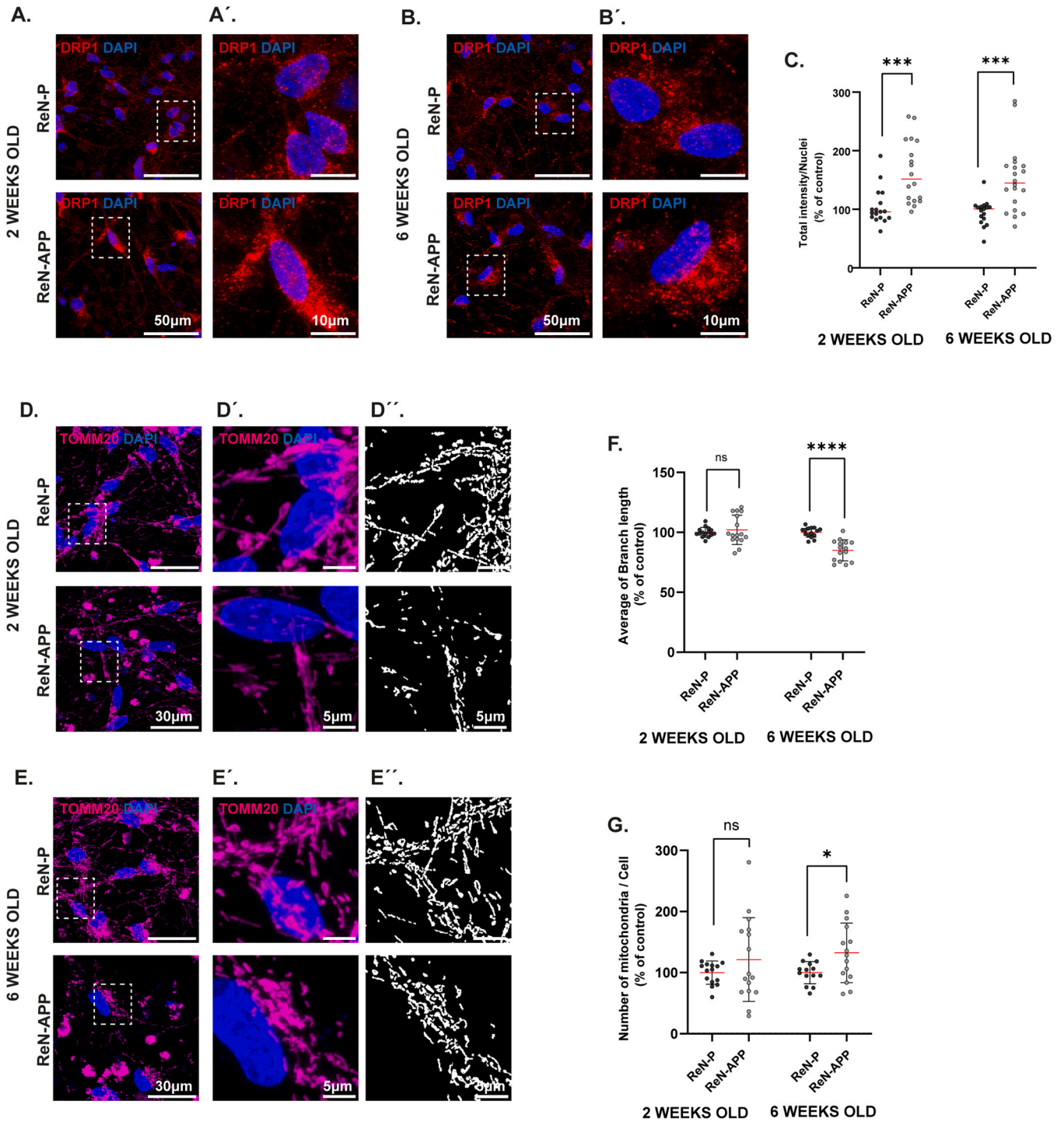

Fig. 3. Disrupted mitochondrial dynamics in early and late-stage APP-expressing cell lines A, B. Immunofluorescence staining of DRP1 (red) and DAPI (blue) nuclei staining in ReN-P and ReN-APP cells at 2 and 6 weeks. Images were taken using a confocal laser microscope (Olympus FV3000). Scale bar: 50 µm. A′, B′: Zoomed-in views of the boxed regions. Scale bar:10 µm. **C.** Quantification of total DRP1 fluorescence intensity normalized to the number of nuclei using CellProfiler. **D, E** Immunofluorescence staining of TOMM20 (magenta) to assess the mitochondrial network at 2 and 6 weeks. Scale bar: 50 µm. D′, E′: Zoomed-in views of the boxed regions. Scale bar: 5 µm, D″ and E″ show MitoSegNet-segmented images of the same regions and share the same scale (5 µm) **F, G** Quantification of average mitochondrial branch length **(F)** and number of mitochondria per cell **(G)** using MitoSegNet. n = 3 biological replicates with N ≥ 5 images per condition. Data are shown as scatter plots with mean ± SD. Normality was assessed using the Shapiro–Wilk test. For comparisons between two groups, normally distributed data with homogenous variances were analyzed using unpaired *t*-tests; when normality or equal variance assumptions were not met, Mann–Whitney tests were used. ns, not significant, *p < 0.05; **p < 0.01; ***p < 0.001, ****p < 0.0001.

TOMM20 and LAMP2, a marker for lysosomes. Mitochondria–lysosome colocalization was quantified by calculating the Manders M1 coefficient, representing the fraction of TOMM20 signal overlapping with LAMP2. After 6 weeks of differentiation, the Manders M1 value was significantly reduced in ReN-APP cells compared to ReN-P controls, indicating impaired mitochondrial delivery to lysosomes (Fig. 4F-G). In contrast, no significant differences were observed at 2 weeks, where control cells exhibited mild but detectable mitochondrial–lysosomal overlap

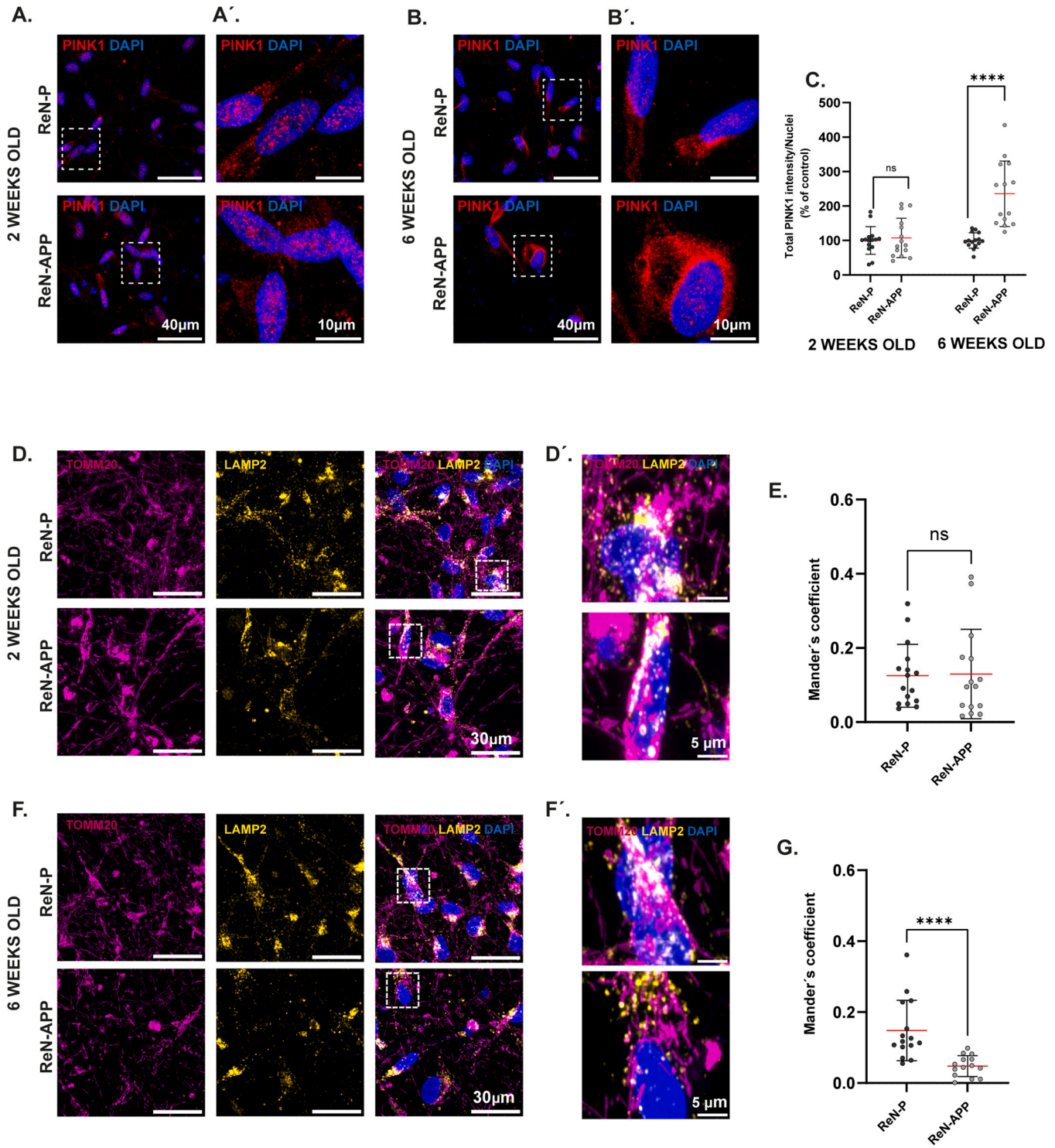

Fig. 4. Impaired mitophagy in the late stage of ReN-APP cells A, B. Immunofluorescence staining of 2 and 6 weeks ReN-P and ReN-APP cells, staining with PINK1 (red) and DAPI (blue) for nuclear staining. Scale bar: 40 µm. **C** Quantification of total PINK1 fluorescence intensity normalized to the number of nuclei for 2 and 6-week time points. **D, F** Immunofluorescence staining of ReN-APP and ReN-P cells using LAMP2 (lysosomal marker, yellow) and TOMM20 (mitochondrial marker) to assess colocalization of mitochondria and lysosome after 2 weeks (D) and 6 weeks (F) of differentiation. Scale bar: 30 µm. **D′, F′** Zoomed-in on the boxed regions in D and F, indicating PINK1/LAMP2 colocalization. Scale bar: 5 µm **E, G** Mander's colocalization coefficient quantifying LAMP2–TOMM20 overlap at 2 weeks (E) and 6 weeks (G), indicating Mito lysosome formation over time. Data are shown as scatter plots with mean ± SD. Normality was assessed using the Shapiro–Wilk test. For comparisons between two groups, normally distributed data with homogenous variances were analyzed using unpaired *t*-tests; when normality or equal variance assumptions were not met, Mann–Whitney tests were used. n = 3 biological replicates with N ≥ 5 images per condition. ns, not significant, *p < 0.05; **p < 0.01; ***p < 0.001, ****p < 0.0001.

(Fig. 4D-E). These findings suggest that although mitophagy is initiated, as shown by the upregulation of PINK1 in ReN-APP cells by 6 weeks, mitochondrial targeting to the lysosome and therefore, degradation is disrupted.

To corroborate the *in vitro* observations in a physiologically relevant *in vivo* system, we employed Tg rats expressing human APP transgene with the Swedish and Indiana mutations. To determine whether cerebral Aβ accumulation alters mitochondrial function, we first determined the production and accumulation of Aβ in soluble (monomers, oligomers, and protofibrils) and insoluble (fibrils and plaques) forms using immunohistochemistry. Immunostaining for Aβ showed the presence of intraneuronal Aβ accumulation in the hippocampus of 3-month-old Tg rats (Fig. 5A), while immunostaining in the hippocampus of 9-month-old Tg rats showed the presence of extracellular Aβ plaques in addition to intraneuronal Aβ accumulation (Fig. 5B). Moreover, human soluble Aβ isoforms 38, 40, and 42 could be detected in hippocampal homogenates of Tg animals of 3 and 9 months of age using a highly sensitive multiplex MSD ELISA. Despite slightly higher levels in Aβ-isoforms 40 and 42, no significant differences in their levels were observed between the two time points (Supplementary Fig. 4A-B). We assessed the level of protein nitrosylation as a marker of oxidative–nitrosative stress damage in total hippocampal fractions and mitochondrial proteins from 3- and 9-month-old rats. Quantitative analysis of 3-NT band intensity, normalized to the appropriate loading control (tubulin for total fraction, TOMM20 for mitochondrial fraction), revealed a significant increase in 3-NT levels in both hippocampal total fraction (Supplementary Fig. 2A-D) and mitochondrial fractions (Fig. 5C-F) from Tg rats compared to WT rats at 9 months of age, while no significant change was observed at 3 months. Moreover, quantitative analysis of DRP1 revealed a significant increase in mitochondrial DRP1 levels in Tg rats compared to WT rats at 9 months of age (Fig. 5G-J). To determine whether this increase reflected a generalized elevation in total DRP1 levels (including cytoplasmic, inactive DRP1) rather than a specific rise in mitochondrial DRP1 (active form), we analyzed the total fraction at both ages. No significant differences in total DRP1 levels between Tg and WT rats at either 3 or 9 months of age were observed (Supplementary Fig. 2E-H).

3.5. The accumulation of Aβ impairs mitophagy flux

After detecting mitochondrial dysfunction in the hippocampus of 9-month-old rats, we were interested in evaluating whether, similar to the *in vitro* data, mitophagy was also altered *in vivo*. To assess the initiation of mitophagy, we measured the expression level of PINK1 in the mitochondrial fraction of both ages. Quantitative analysis revealed a significant increase in mitochondrial PINK1 levels in Tg rats compared to WT rats at 9 months of age, while no significant differences were observed at the 3-month time point (Fig. 6A-D). In contrast, the overall expression of PINK1 was not elevated in the total fractions at both ages (Supplementary Fig. 3A-D). This indicates that the increase in PINK1 is specific to its mitochondria-bound form and elevated levels of mitochondria-associated PINK1 are strongly suggestive of mitophagy activation at this age. Further, we were interested in evaluating the progression of mitophagy, specifically the transport of mitochondria to lysosomes. Western blotting of p62 (an early marker of autophagosomes) in total fractions showed a significant increase in p62 levels in hippocampal samples from Tg rats compared to WT rats at 9 months of age, while no significant differences were observed at the 3-month time point (Supplementary Fig. 3E-H). To assess whether the increase in total p62 correlates with an accumulation of p62 bound to dysfunctional mitochondria, we analyzed the mitochondrial fraction at both ages. The levels of the band corresponding to p62 were increased in mitochondrial fractions from 9-month-old Tg rats compared to WT rats, but no differences were observed in 3-month-old samples (Fig. 7A-D). These results suggest an accumulation of dysfunctional mitochondria and/or activation of the mitophagy pathway in response to mitochondrial dysfunction in aged Tg rats.

To further evaluate the progression of mitophagy, we performed Western blotting followed by immunoblotting of the LC3-II/LC3-I ratio (a late marker of autophagosomes) in total fractions. A significant increase in LC3-II/LC3-I levels was observed in hippocampal samples from Tg rats compared to WT rats at 9 months of age, while no significant differences were observed at the 3-month time point (Fig. 7E-H). These findings suggest that although mitophagy is initiated in hippocampal samples at 9-month-old animals, mitochondrial degradation is impaired, possibly due to deficient mitochondrial trafficking or defective lysosomal fusion. Our results support that the accumulation of Aβ and oxidative stress may impact mitochondrial degradation.

4. Discussion

In this study, we modelled amyloidosis using both an *in vitro* human neural progenitor system (ReN cells) and an *in vivo* transgenic rat model carrying FAD-relevant APP mutations. The ReN-APP cell line, generated by stable expression of the Swedish and London APP variants (Choi et al., 2014; Donato et al., 2007), displayed an elevated Aβ42/40 ratio at both 2 and 6 weeks, consistent with a key pathological hallmark of AD (Doecke et al., 2020). The transgenic rat model, carrying the Swedish and Indiana APP mutations, has been shown to develop intraneuronal Aβ accumulation and amyloid plaques, thereby providing a complementary *in vivo* system to study disease progression.

Mitochondrial dysfunction induced by Aβ is well documented. Multiple studies have demonstrated that Aβ accumulation impairs mitochondrial function, oxidative balance, and dynamics (de la Cueva et al., 2022; Wang et al., 2008). Novack and colleagues demonstrated that supercomplexes containing complex I in the hippocampus are destabilized in a rat model of cerebral amyloidosis, leading to impaired activity and nitro-oxidative stress (Novack et al., 2025). In line with this body of evidence, our previous findings showed that Aβ treatment leads to mitochondrial impairment in ReN cell (Motamed et al., 2025). Building on this, in the present study we aimed to assess mitochondrial performance, dynamics, and mitophagy at both early and late stages in environments with sustained Aβ release, using complementary *in vitro* and *in vivo* models.

In the initial stages of AD, mitochondria exhibit subtle impairments in energy metabolism, increased oxidative stress, and altered network dynamics, which may occur while membrane potential is still preserved (Picone et al., 2014; Wang et al., 2025, 2014). As the disease progresses, these early changes advance to more severe defects, including loss of mitochondrial membrane potential, increased permeability, and excessive ROS production, reflecting bioenergetic failure that ultimately leads to synaptic dysfunction and neuronal death (Hauptmann et al., 2009; Xie et al., 2013). Therefore, this work focused on early and late mitochondrial status in the context of pathological Aβ release.

We observed elevated mitochondrial ROS levels already in early stages in 2-week-old ReN-APP cells, without a concomitant change in the GSH/GSSG ratio. This supports our assumption that 2 weeks of differentiation represents the early stages of Aβ-mediated cellular damage and suggests that, at this point, the antioxidant defense system was still functional and able to balance the initial oxidative stress. Notably, this early oxidative shift coincided with an elevated Aβ42/40 ratio, indicating the early onset of amyloid-related stress, and indicates that in ReN-APP cells, Aβ accumulation leads to an increased ROS production. This is in line with the initial increased oxidative stress caused by Aβ, which has been shown to generate ROS in the presence of the transition metals copper and iron *in vitro* (Smith et al., 2007). Moreover, 2-week-old ReN-APP cells also showed significantly increased DRP1 levels, without a morphological correlate. DRP1 is a key protein that regulates mitochondrial fission, whose expression and activity are upregulated by ROS (Cid-Castro and Morán, 2021) and following chemically-induced oxidative stress in neurons (Chen et al., 2021) thus, it is considered an early marker of mitochondrial oxidative stress.

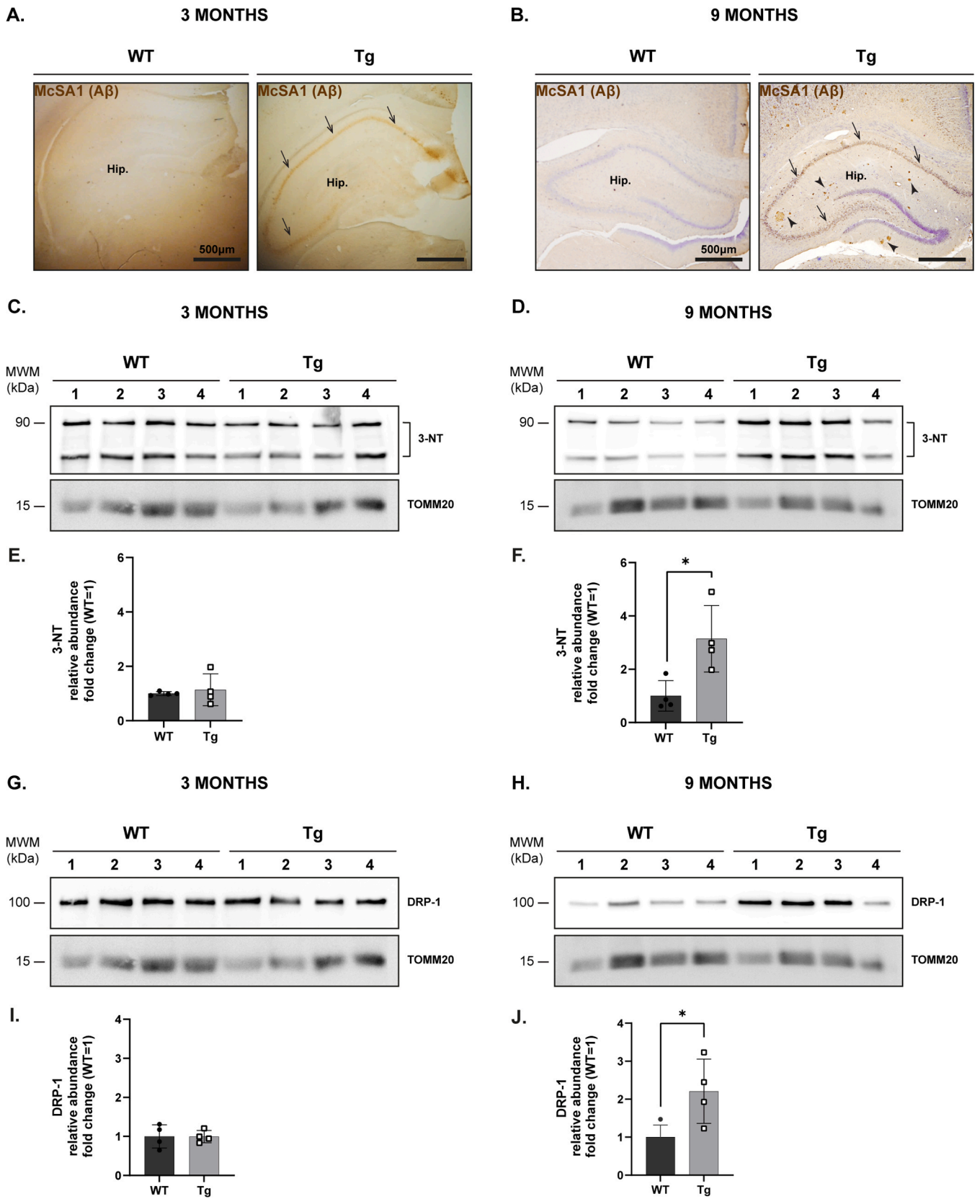

(caption on next page)

Fig. 5. Progressive hippocampal Aβ accumulation *in vivo* drives nitro-oxidative stress and alters mitochondrial fission dynamics A. Representative microphotographs of Wild type (WT, left panel) and Tg rat brains (right panel) showing intraneuronal accumulation of Aβ (black arrows) detected in the 3-month-old Tg rats. **B** Representative microphotograph showing intraneuronal accumulation of Aβ (black arrows) and extracellular plaques (black arrowheads) detected in the 9-month-old Tg rats. Hippocampus (Hip) shows intense McSA1 immunoreactivity in Tg (right panel) as compared to age-matched WT rats (left panel). Scale bar: 500 μm. **C, D** Representative Western blots of mitochondrial fractions from WT (n = 4) and Tg (n = 4) rats at 3 **(C)** and 9 months **(D)** hippocampi, using an anti-3-nitrotyrosine (3-NT) antibody. TOMM20 was used as a loading control. **E, F:** Quantification of relative abundance of 3-NT protein levels in Tg compared to WT, presented as fold change, at 3 months **(E)** and 9 months **(F). G, H** Representative Western blots of mitochondrial fractions from WT (n = 4) and Tg (n = 4) rats at 3 **(G)** and 9 months **(H)**, probed with an anti-DRP1 antibody. TOMM20 was used as loading control **(I, J).** Bars show relative abundance of DRP1 protein levels in mitochondrial fractions from Tg compared to WT rats, expressed as fold change, at 3 months **(I)** and 9 months **(J).** Statistical analysis was performed using the parametric unpaired two-tailed *t*-test $*p < 0.05$. All data are presented as mean ± SEM with individual data overlaid. Panels 5 C, 5 G, and 6A share the same TOMM20 housekeeping/loading control, as they derive from the same membrane; the uncropped membrane is shown in Fig. S5A. In addition, Panels 5D, 5 H, and 6B share the same TOMM20 housekeeping/loading control from the corresponding membrane, shown uncropped in Fig. S5B.

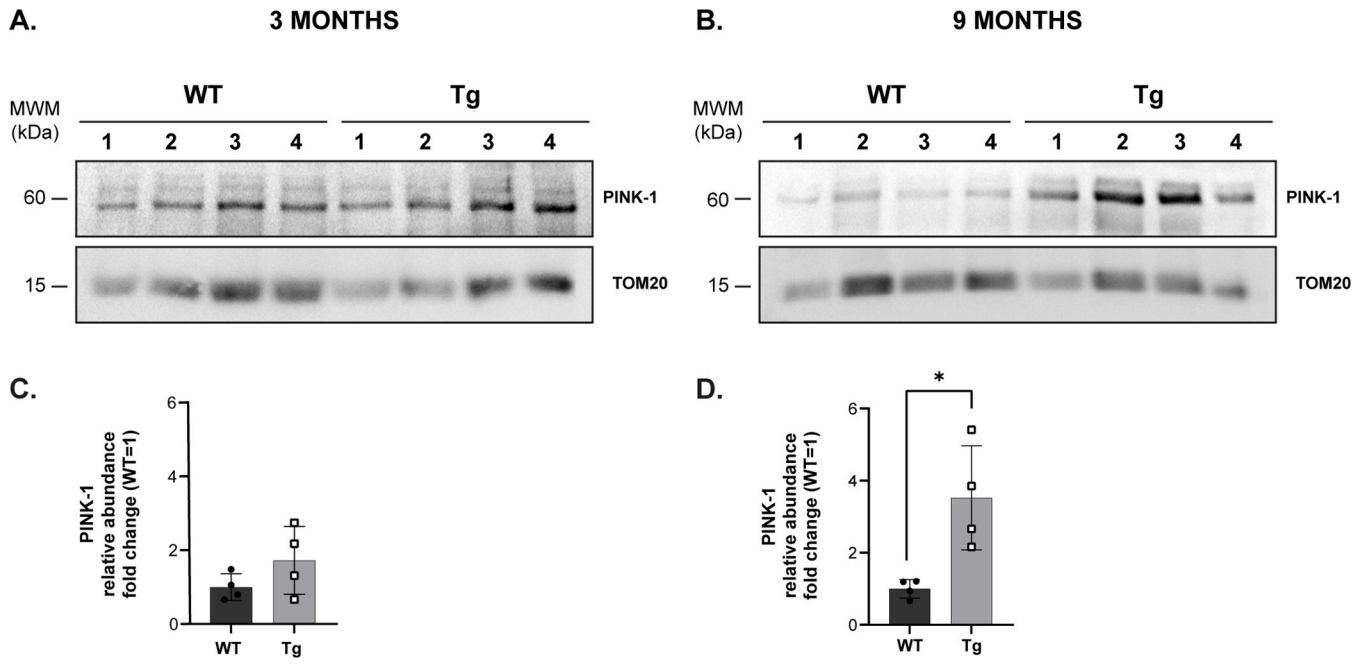

Fig. 6. The accumulation of Aβ triggers mitophagy in the later stage of the *in vivo* model A, B. Representative Western blots of hippocampal mitochondrial fractions from WT (n = 4) and Tg (n = 4) rats at 3 months (A) and 9 months (B) using anti-PINK1 antibody, and TOMM20 as loading control. **C, D** Bars show relative abundance of PINK1 protein levels from WT and Tg rats at 3 months (C) and 9 months (D), expressed as fold change compared to WT. Statistical analysis was performed using the parametric unpaired two-tailed Welch's *t*-test $*p < 0.05$. Data are shown as mean ± SEM with individual data points overlaid.

In vivo results obtained with 3-month-old APP Tg rats, considered a model of early cerebral amyloidosis, failed to show oxidative stress as determined by the cellular levels of protein-resident-nitrotyrosine (3-NT), despite the observed increase in Aβ peptides and in the Aβ 42/40 ratio. The results obtained at early time points (2 weeks and 3 months for *in vitro* and *in vivo*, respectively) suggest that the initial step in Aβ-mediated cellular damage is a subclinical increase of ROS, only detectable *in vitro* as the antioxidant response mechanisms are still intact and probably prevent the covalent modification of proteins, such as the formation of 3-NT. This observation is consistent with previous findings in the McGill-APP Tg rat model, where intracellular Aβ accumulation in 5-month-old animals triggered early oxidative stress, DNA damage, and maladaptive expression of synaptic plasticity, related genes in hippocampal neurons, occurring months before the onset of extracellular Aβ plaque deposition and independently of overt cell death (Foret et al., 2024). In contrast, at later timepoints, the antioxidative defense mechanisms seem to be overruled and mitochondrial protein modifications become evident both *in vitro* and *in vivo*.

In ReN-APP cell cultures maintained for 6 weeks, sustained ROS production appeared to overwhelm the cellular antioxidant defense system, as indicated by a significant decline in the GSH/GSSG ratio. This redox shift may reflect reduced buffering capacity and increased the damage elicited by oxidative stress, resulting in lower mitochondrial membrane potential. Impaired mitochondrial function is often followed by disruptions in mitochondrial dynamics (Li et al., 2025). As differentiation progressed to 6 weeks and oxidative stress became more prominent, DRP1 levels remained elevated in ReN-APP cells and led to mitochondrial fragmentation, detected as a reduction of branch length and an increase in mitochondrial number. The findings are further supported by the *in vivo* data showing oxidative protein damage (high 3-NT levels) and elevated DRP1 levels in isolated mitochondria at 9-month-old APP Tg rats. These findings are consistent with published results in the same animal model, showing that the stress markers protein-bound-hydroxynonenal (HNE) and protein-resident -nitrotyrosine (3-NT) were increased in APP Tg brains (Wilson et al., 2018). Proteomic analysis of the hippocampus of 12-month-old Tg rats revealed alterations in pathways related to energy metabolism and decreased ATP production as well as alterations in the degree of lipid peroxidation, and changes in the oxidized/reduced glutathione ratio, indicating oxidative stress(Do Carmo et al., 2018). They are also supported by publications describing DRP-1 phosphorylation and mitochondrial fission in an AD-like rat model (Cho et al., 2012) as well as by findings in the brains of AD patients showing a critical role for DRP1 in promoting mitochondrial fragmentation and contributing to synaptic damage (Manczak et al., 2011). Moreover, published data have shown mitochondrial defects in AD models, increased mitochondrial

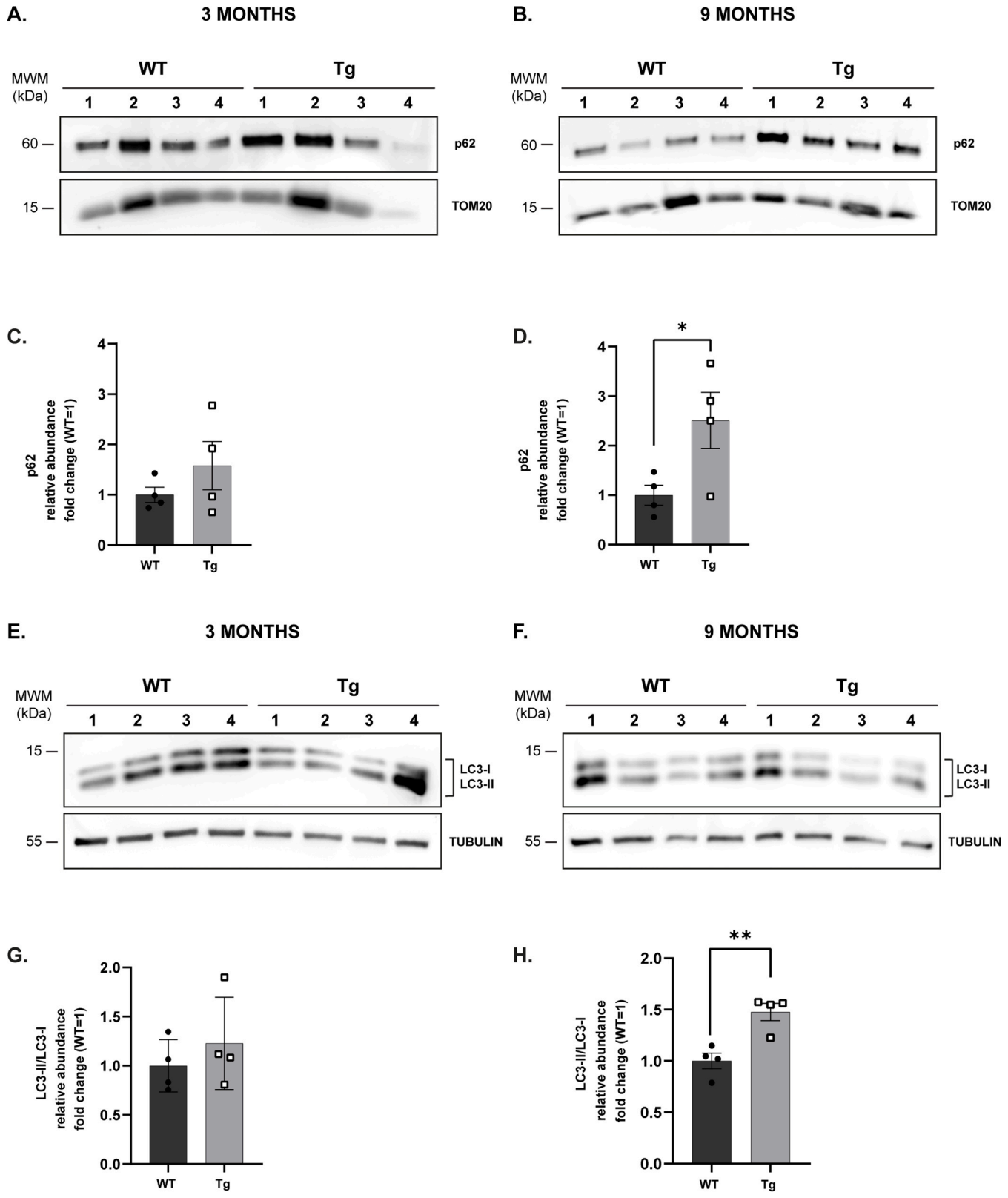

Fig. 7. The Aβ accumulation impairs p62–LC3-mediated sequestration of mitochondria *in vivo* A, B. Representative Western blots of hippocampal mitochondrial fractions from WT (n = 4) and Tg (n = 4) rats at 3 months (A) and 9 months (B), probed with an anti-p62 antibody. TOMM20 was used as a loading control. **C, D** Bars show relative abundance of p62 protein levels from WT and Tg rats at 3 months (C) and 9 months (D), expressed as fold change compared to WT. **E, F** Western blot analysis of LC3 isoforms in total fractions from wild-type (WT) and APP transgenic (Tg) mice at 3 months (E) and 9 months (F) hippocampi. **G, H** Quantification of LC3-II/LC3-I ratios is shown for 3 months (G) and 9 months (H). While no significant change was observed at 3 months, a significant increase in LC3-II/LC3-I ratio was detected in Tg mice at 9 months, indicating an accumulation of autophagosomes or impaired autophagic flux at later stages. Statistical analysis was performed using either parametric (unpaired two-tailed Welch's *t*-test) or non-parametric (Mann–Whitney *U* test). Data are shown as mean ± SEM with individual data points overlaid. ns, not significant, *p < 0.05; **p < 0.01; ***p < 0.001, ****p < 0.0001.

fragmentation, and shorter branch length (Chen et al., 2022) and that in HT-22 mouse hippocampal neuronal cells, exposure to Aβ causes mitochondrial fragmentation and an increase in mitochondrial number, revealed by high-resolution STED microscopy (Golovynska et al., 2025).

Damaged mitochondria are physiologically removed by mitophagy. However, AD is also characterized by an early pathological feature of impaired mitophagy that leads to the accumulation of damaged mitochondria (Chakravorty et al., 2019; Xie et al., 2020). To understand the mitophagy in our systems, we investigated the expression of PINK1, a key cellular sensor of damaged mitochondria, recruiting them for mitophagy. As expected, due to the detected increase in the number of damaged mitochondria, PINK1 levels were elevated at the late (but not the early) time points *in vitro* and *in vivo*. This indicates that mitophagy is activated in response to mitochondrial damage subsequent to Aβ accumulation. This is in concordance with findings from Roca-Agujetas et al (2021)., who investigated Aβ-induced mitophagy in SH-SY5Y neuroblastoma cells and primary neurons derived from SREBF2-overexpressing mice, showing that Aβ exposure stimulates PINK1 and the formation of LC3B-positive mitophagosomes (Roca-Agujetas et al., 2021). While previous work, reviewed by Goudarzi et al., has established that Aβ can disrupt Parkin-mediated mitophagy (Goudarzi et al., 2021), our study extends these findings by mapping how chronic, endogenous Aβ production drives a stage-dependent sequence of redox imbalance, mitochondrial network remodeling, and impaired mitophagy flux in genetically defined APP models, both in human ReN-APP cultures and in APP transgenic rats. However, higher expression of PINK1 does not guarantee increased mitophagy. Our data indicate that despite elevated PINK1 levels, the mitophagic flux is impaired. Specifically, low colocalization of the mitochondrial marker TOMM20 with the lysosomal marker LAMP2 in ReN-APP cells, and retention of p62 in the mitochondrial fraction in Tg rat brains, suggests inefficient mitolysosome formation and thus mitophagic clearance. These data are consistent with a reduced co-localization and have a clinical correlate, as similar results were reported by Fang et al.(2019), showing reduced co-localization of TOMM20 with LAMP2 in postmortem human hippocampal tissue of an AD patient, indicating impaired mitophagy clearance (Fang et al., 2019).

Taken together, our data suggest that sustained Aβ secretion (detectable as an early increase in the Aβ42/40 ratio) drives progressive redox imbalance, mitochondrial damage, impaired mitophagy, and cellular loss that can be detected *in vitro* and *in vivo* and that correlates with pathological findings in AD patients. Mitochondrial damage seems to be a key event, as dysfunctional mitochondria accumulate, resulting in neuronal loss, consistent with features of neurodegeneration (Bayer, 2010; Wasilewski et al., 2022). This finding supports Han et al.(2017), who demonstrated that extracellular Aβ42 treatment of primary mouse cortical neurons led to increased mitochondrial fission (via upregulation of DRP1), decreased mitochondrial fusion proteins (Mfn1, Mfn2, OPA1), loss of mitochondrial membrane potential, elevated ROS, and activation of mitophagy (indicated by PINK1 and LC3B expression) that collectively contribute to neuronal apoptosis (Han et al., 2017).

By combining human progenitor cells and a transgenic rat model, this study provides complementary insights into the progression of mitochondrial dysfunction in the context of progressive Aβ accumulation typical of AD. Although the precise causal links in AD cannot yet be fully established due to its complexity, our stage-based models identify both early and late molecular alterations in mitochondrial homeostasis. These alterations may serve as a basis for preclinical investigations and open the possibility of therapeutic targeting at initial disease stages. Despite these strengths, several limitations should be noted. This study was designed to compare early and late stages of Aβ-driven pathology in complementary human and rat models. While this approach reveals a clear stage-dependent phenotype, additional intermediate time points would further refine the temporal sequence of redox imbalance, mitochondrial remodeling, and mitophagy disruption. In addition, *in vitro* analyses were performed in a mixed neuro-glial culture without cell-type- or compartment-specific separation; future work will quantify mitochondrial morphology and mitophagy separately in neurons versus astrocytes and within soma versus neuritic processes.

CRediT authorship contribution statement

A. Claudio Cuello: Writing – review & editing, Writing – original draft, Conceptualization. **Laura Morelli:** Writing – review & editing, Writing – original draft, Supervision, Investigation, Funding acquisition, Conceptualization. **Sonia Do Carmo:** Writing – review & editing, Investigation, Data curation. **Zahra Motamed:** Writing – review & editing, Writing – original draft, Visualization, Methodology, Investigation, Formal analysis, Data curation, Conceptualization. **Laura Suter-Dick:** Writing – review & editing, Supervision, Resources, Project administration, Investigation, Funding acquisition, Conceptualization. **Carine Gaiser:** Writing – review & editing, Writing – original draft, Methodology, Investigation, Data curation, Conceptualization. **Corina Garcia:** Writing – review & editing, Writing – original draft, Methodology, Investigation. **Gisela Novack:** Writing – review & editing, Writing – original draft, Visualization, Methodology, Investigation, Formal analysis, Data curation. **Daniel Heutschi:** Writing – original draft, Methodology, Formal analysis, Data curation.

Acknowledgements

The authors thank the funding by the Applied Sciences University Northwestern Switzerland (FHNW) that financed the research with an internal grant (FHNW, School of Life Sciences) and as well as Agencia Nacional de Promoción Científica y Tecnológica (PICT2019–0656 and PICT2022–00227 to L.M) and EULAC – Health Neurodegeneration JOINT CALL 20162017 “Fatzheimer” (to L.M.) for supporting the in vivo experiments. We are very grateful to Prof. Eduardo M. Castaño for his scientific support and the critical review of the manuscript as well as to Cecilia Rotondaro for her support with the immunohistochemistry.

Gisela V Novack received support from a CONICET (Argentina) doctoral scholarship and a SEMP (student Exchange) scholarship from the FHNW School of Life Sciences in Muttenz, Switzerland. The authors would like to thank Rotary International and Rotary Club for facilitating Gisela V Novack's accommodation in Switzerland during her stay.

Disclosure statement

The authors have no actual or potential conflicts of interest.

Appendix A. Supporting information

Supplementary data associated with this article can be found in the online version at doi:10.1016/j.neurobiolaging.2026.01.006.

References

Bartolome, F., de la Cueva, M., Pascual, C., Antequera, D., Fernandez, T., Gil, C., et al., 2018. Amyloid β-induced impairments on mitochondrial dynamics, hippocampal neurogenesis, and memory are restored by phosphodiesterase 7 inhibition. Alzheimers Res Ther. 10, 24. https://doi.org/10.1186/s13195-018-0352-4.

Bayer, T.A., 2010. Wirths O. Intracellular accumulation of amyloid-beta – a predictor for synaptic dysfunction and neuron loss in Alzheimer’s disease. Front. Aging Neurosci. 2:8. https://doi.org/10.3389/fnagi.2010.00008.

Bordi, M., Berg, M.J., Mohan, P.S., Peterhoff, C.M., Alldred, M.J., Che, S., et al., 2016. Autophagy flux in CA1 neurons of Alzheimer hippocampus: increased induction overburdens failing lysosomes to propel neuritic dystrophy. Autophagy 12 (12), 2467–2483. https://doi.org/10.1080/15548627.2016.1239003.

Butterfield, D.A., Boyd-Kimball, D., 2020. Mitochondrial oxidative and nitrosative stress and Alzheimer disease. Antioxidants (Basel) 9 (9), 818. https://doi.org/10.3390/antiox9090818.

Cadenas, E., Boveris, A., 1980. Enhancement of hydrogen peroxide formation by protophores and ionophores in antimycin-supplemented mitochondria. Biochem. J. 188, 31–37. https://doi.org/10.1042/bj1880031.

Calvo-Rodriguez, M., Kharitonova, E.K., Snyder, A.C., Hou, S.S., Sanchez-Mico, M.V., Das, S., et al., 2024. Real-time imaging of mitochondrial redox reveals increased mitochondrial oxidative stress associated with amyloid β aggregates in vivo in a mouse model of Alzheimer's disease. Mol. Neurodegener. 19 (1), 6. https://doi.org/10.1186/s13024-024-00702-2.

Caspersen, C., Wang, N., Yao, J., Sosunov, A., Chen, X., Lustbader, J.W., et al., 2005. Mitochondrial Abeta: a potential focal point for neuronal metabolic dysfunction in Alzheimer's disease. FASEB J. 19 (14), 2040–2041. https://doi.org/10.1096/fj.05-3735fje.

Chakravorty, A., Jetto, C.T., Manjithaya, R., 2019. Dysfunctional mitochondria and mitophagy as drivers of Alzheimer's disease pathogenesis. Front. Aging Neurosci. 11, 311. https://doi.org/10.3389/fnagi.2019.00311.

Chen, D., Yu, W., Aitken, L., Gunn-Moore, F., 2022. Willin/FRMD6 mediates mitochondrial dysfunction relevant to neuronal Aβ toxicity. Cells 11 (19), 3140. https://doi.org/10.3390/cells11193140.

Chen, N., Guo, Z., Luo, Z., Zheng, F., Shao, W., Yu, G., et al., 2021. Drp1-mediated mitochondrial fission contributes to mitophagy in paraquat-induced neuronal cell damage. Environ. Pollut. 272, 116413. https://doi.org/10.1016/j.envpol.2020.116413.

Cho, M.H., Kim, D.H., Choi, J.E., Chang, E.J., 2012. Yoon SY. Increased phosphorylation of dynamin-related protein 1 and mitochondrial fission in okadaic acid-treated neurons, 2012;0 Brain Res. 1454. https://doi.org/10.1016/j.brainres.2012.03.010.

Choi, S.H., Kim, Y.H., Hebisch, M., Sliwinski, C., Lee, S., D'Avanzo, C., et al., 2014. A three-dimensional human neural cell culture model of Alzheimer's disease. Nature 515 (7526), 274–278. https://doi.org/10.1038/nature13800.

Cid-Castro, C., Morán, J., 2021. Differential ROS-mediated phosphorylation of Drp1 in mitochondrial fragmentation induced by distinct cell death conditions in cerebellar granule neurons. Oxid. Med. Cell Longev. 2021, 8832863. https://doi.org/10.1155/2021/8832863.

de la Cueva, M., Antequera, D., Ordoñez-Gutierrez, L., Wandosell, F., Camins, A., Carro, E., et al., 2022. Amyloid-β impairs mitochondrial dynamics and autophagy in Alzheimer's disease experimental models. Sci. Rep. 12 (1), 10092. https://doi.org/10.1038/s41598-022-13683-3.

Devi, L., Prabhu, B.M., Galati, D.F., Avadhani, N.G., Anandatheerthavarada, H.K., 2006. Accumulation of amyloid precursor protein in the mitochondrial import channels of human Alzheimer's disease brain is associated with mitochondrial dysfunction. J. Neurosci. 26 (35), 9057–9068. https://doi.org/10.1523/JNEUROSCI.1469-06.2006.

Do Carmo, S., Crynen, G., Paradis, T., Reed, J., Iulita, M.F., Ducatenzeiler, A., et al., 2018. Hippocampal proteomic analysis reveals distinct pathway deregulation profiles at early and late stages in a rat model of Alzheimer's-like amyloid pathology. Mol. Neurobiol. 55 (4), 3451–3476. https://doi.org/10.1007/s12035-017-0580-9.

Doecke, J.D., Pérez-Grijalba, V., Fandos, N., Fowler, C., Villemagne, V.L., Masters, C.L., et al., 2020. AIBL Research Group. Total Aβ_{42}/Aβ_ {40} ratio in plasma predicts amyloid-PET status, independent of clinical AD diagnosis. e1580–e1591 Neurology 94 (15), e1580–e1591. https://doi.org/10.1212/WNL.0000000000009240.

Donato, R., Miljan, E.A., Hines, S.J., Aouabdi, S., Pollock, K., Patel, S., et al., 2007. Differential development of neuronal physiological responsiveness in two human neural stem cell lines. BMC Neurosci. 8, 36. https://doi.org/10.1186/1471-2202-8-36.

Fang, E.F., Hou, Y., Palikaras, K., Adriaanse, B.A., Kerr, J.S., Yang, B., et al., 2019. Mitophagy inhibits amyloid-β and tau pathology and reverses cognitive deficits in models of Alzheimer's disease. Nat. Neurosci. 22 (3), 401–412. https://doi.org/10.1038/s41593-018-0332-9.

Fischer, C.A., Besora-Casals, L., Rolland, S.G., Haeussler, S., Singh, K., Duchen, M., et al., 2020. MitoSegNet: easy-to-use deep learning segmentation for analyzing mitochondrial morphology. iScience 23 (10), 101601. https://doi.org/10.1016/j.isci.2020.101601.

Flannery, P.J., Trushina, E., 2019. Mitochondrial dynamics and transport in Alzheimer's disease. Mol. Cell Neurosci. 98, 109–120. https://doi.org/10.1016/j.mcn.2019.06.009.

Foret, M.K., Orciani, C., Welikovitch, L.A., Huang, C., Cuello, A.C., Do Carmo, S., 2024. Early oxidative stress and DNA damage in Aβ-burdened hippocampal neurons in an Alzheimer's-like transgenic rat model. Commun. Biol. 7 (1), 861. https://doi.org/10.1038/s42003-024-06552-4.

Golovynska, I., Chen, Q., Stepanov, Y.V., Lin, D., Qu, J., 2025. Amyloid-induced mitochondrial network disruption in neurons monitored by STED super-resolution imaging. Front. Cell Dev. Biol. 13, 1610204. https://doi.org/10.3389/fcell.2025.1610204.

Goudarzi, S., Hosseini, A., Abdollahi, M., Haghi-Aminjan, H., 2021. Insights into Parkin-mediated mitophagy in Alzheimer's disease: a systematic review, 13 Front. Aging Neurosci. 13, 674071. https://doi.org/10.3389/fnagi.2021.674071.

Han, X.J., Hu, Y.Y., Yang, Z.J., Jiang, L.P., Shi, S.L., Li, Y.R., et al., 2017. Amyloid β-42 induces neuronal apoptosis by targeting mitochondria. Mol. Med. Rep. 16 (4), 4521–4528. https://doi.org/10.3892/mmr.2017.7203.

Hansson Petersen, C.A., Alikhani, N., Behbahani, H., Wiehager, B., Pavlov, P.F., Alafuzoff, I., et al., 2008. The amyloid beta-peptide is imported into mitochondria via the TOM import machinery and localized to mitochondrial cristae. Proc. Natl. Acad. Sci. USA 105 (35), 13145–13150. https://doi.org/10.1073/pnas.0806192105.

Hauptmann, S., Scherping, I., Dröse, S., Brandt, U., Schulz, K.L., Jendrach, M., et al., 2009. Mitochondrial dysfunction: an early event in Alzheimer pathology accumulates with age in AD transgenic mice. Neurobiol. Aging 30 (10), 1574–1586. https://doi.org/10.1016/j.neurobiolaging.2007.12.005.

Hein, Z.M., Vishnumukkala, T., Karikalan, B., Alkatiri, A., Hussan, F., Jagadeesan, S., et al., 2025. Autophagy and Alzheimer's disease: mechanisms and impact beyond the brain. Cells 14 (12), 911. https://doi.org/10.3390/cells14120911.

Hirai, K., Aliev, G., Nunomura, A., Fujioka, H., Russell, R.L., Atwood, C.S., et al., 2001. Mitochondrial abnormalities in Alzheimer's disease. J. Neurosci. 21 (9), 3017–3023. https://doi.org/10.1523/JNEUROSCI.21-09-03017.2001.

Jha, P., Wang, X., Auwerx, J., 2016. Analysis of mitochondrial respiratory chain supercomplexes using blue native polyacrylamide gel electrophoresis (BN-PAGE). Curr. Protoc. Mouse Biol. 6, 1–14. https://doi.org/10.1002/9780470942390.mo150182.

Kandimalla, R., Reddy, P.H., 2016. Multiple faces of dynamin-related protein 1 and its role in Alzheimer's disease pathogenesis. Biochim. Biophys. Acta Mol. Basis Dis. 1862, 814–828. https://doi.org/10.1016/j.bbadis.2015.12.018.

Leal, M.C., Dorfman, V.B., Gamba, A.F., Frangione, B., Wisniewski, T., Castaño, E.M., et al., 2006. Plaque-associated overexpression of insulin-degrading enzyme in the cerebral cortex of aged transgenic tg2576 mice with Alzheimer pathology. J. Neuropathol. Exp. Neurol. 65, 976–987. https://doi.org/10.1097/01.jnen.0000235853.70092.ba.

Leon, W.C., Canneva, F., Partridge, V., Allard, S., Ferretti, M.T., DeWilde, A., et al., 2010. A novel transgenic rat model with a full Alzheimer's-like amyloid pathology displays pre-plaque intracellular amyloid-beta-associated cognitive impairment. J. Alzheimers Dis. 20, 113–126. https://doi.org/10.3233/JAD-2010-1349.

Li, X., Wu, Z., Si, X., Li, J., Wu, G., Wang, M., 2025. The role of mitochondrial dysfunction in the pathogenesis of Alzheimer's disease and future strategies for targeted therapy. Eur. J. Med. Res. 30, 434. https://doi.org/10.1186/s40001-025-02699-w.

LI-COR. Quantitative Western blot analysis with replicate samples [web]. 2018.

Manczak, M., Calkins, M.J., Reddy, P.H., 2011. Impaired mitochondrial dynamics and abnormal interaction of amyloid beta with mitochondrial protein Drp1 in neurons from patients with Alzheimer's disease: implications for neuronal damage. Hum. Mol. Genet. 20, 2495–2509. https://doi.org/10.1093/hmg/ddr139.

Martín-Maestro, P., Gargini, R., Sproul, A.A., García, E., Antón, L.C., Noggle, S., et al., 2017. Mitophagy failure in fibroblasts and iPSC-derived neurons of Alzheimer's disease-associated presenilin 1 mutation. Front. Mol. Neurosci. 10, 291. https://doi.org/10.3389/fnmol.2017.00291.

Martín-Maestro, P., Sproul, A., Martinez, H., Paquet, D., Gerges, M., Noggle, S., et al., 2019. Autophagy induction by bexarotene promotes mitophagy in presenilin 1 familial Alzheimer's disease iPSC-derived neural stem cells. Mol. Neurobiol. 56, 8220–8236. https://doi.org/10.1007/s12035-019-01665-y.

Martino Adami, P.V., Quijano, C., Magnani, N., Galeano, P., Evelson, P., Cassina, A., et al., 2017. Synaptosomal bioenergetic defects are associated with cognitive impairment in a transgenic rat model of early Alzheimer's disease. J. Cereb. Blood Flow. Metab. 37, 69–84. https://doi.org/10.1177/0271678X15615132.

Martino Adami, P.V., Nichtová, Z., Weaver, D.B., Bartok, A., Wisniewski, T., Jones, D.R., et al., 2019. Perturbed mitochondria-ER contacts in live neurons that model the amyloid pathology of Alzheimer's disease. J. Cell Sci. 132, jcs229906. https://doi.org/10.1242/jcs.229906.

Mary, A., Eysert, F., Checler, F., Chami, M., 2023. Mitophagy in Alzheimer's disease: molecular defects and therapeutic approaches. Mol. Psychiatry 28, 202–216. https://doi.org/10.1038/s41380-022-01631-6.

Motamed A., et al. Pathogenic exosomal cargo contributes to Alzheimer's disease propagation. Dis Model Mech. Unpublished results. 2025.

Novack, G.V., Galeano, P., Defelipe, L.A., Campanelli, L., Campuzano, K.S., Rotondaro, C., et al., 2025. The supramolecular architecture of mitochondrial complex I in the rat brain is altered by Alzheimer's-like cerebral amyloidosis. J. Neurochem. 169, e70017. https://doi.org/10.1111/jnc.70017.

Picone, P., Nuzzo, D., Caruana, L., Scafidi, V., Di Carlo, M., 2014. Mitochondrial dysfunction: different routes to Alzheimer's disease therapy. Oxid. Med. Cell Longev. 2014, 780179. https://doi.org/10.1155/2014/780179.

Pszczołowska, M., Walczak, K., Miśków, W., Mroziak, M., Chojdak-Łukasiewicz, J., Leszek, J., et al., 2024. Mitochondrial disorders leading to Alzheimer's disease—perspectives of diagnosis and treatment. GeroScience 46, 2977–2988. https://doi.org/10.1007/s11357-024-01118-y.

Roca-Agujetas, V., Barbero-Camps, E., De Dios, C., Podlesniy, P., Abadin, X., Morales, A., et al., 2021. Cholesterol alters mitophagy by impairing optineurin recruitment and lysosomal clearance in Alzheimer's disease. Mol. Neurodegener. 16 (1), 15. https://doi.org/10.1186/s13024-021-00435-6.

Safiri, S., Ghaffari Jolfayi, A., Fazlollahi, A., Morsali, S., Sarkesh, A., Daei Sorkhabi, A., et al., 2024. Alzheimer's disease: a comprehensive review of epidemiology, risk factors, symptoms, diagnosis, management, caregiving, advanced treatments and associated challenges. Front. Med. 11, 1474043. https://doi.org/10.3389/fmed.2024.1474043.

Schneider, C.A., Rasband, W.S., Eliceiri, K.W., 2012. NIH Image to ImageJ: 25 years of image analysis. Nat. Methods 9 (7), 671–675. https://doi.org/10.1038/nmeth.2089.

Smith, D.G., Cappai, R., Barnham, K.J., 2007. The redox chemistry of the Alzheimer's disease amyloid beta peptide. Biochim. Biophys. Acta Biomembr. 1768, 1976–1990. https://doi.org/10.1016/j.bbamem.2007.02.002.

Song, N., Mei, S., Wang, X., Hu, G., Lu, M., 2024. Focusing on mitochondria in the brain: from biology to therapeutics. Transl. Neurodegener. 13, 23. https://doi.org/10.1186/s40035-024-00409-w.

Wang, H., Zhang, T., Ge, X., Chen, J., Zhao, Y., Fu, J., 2020. Parkin overexpression attenuates Aβ-induced mitochondrial dysfunction in HEK293 cells by restoring impaired mitophagy. Life Sci. 244, 117322. https://doi.org/10.1016/j.lfs.2020.117322.

Wang, S., Liao, Z., Zhang, Q., Han, X., Liu, C., Wang, J., 2025. Mitochondrial dysfunction in Alzheimer's disease: a key frontier for future targeted therapies. Front. Immunol. 15, 1484373. https://doi.org/10.3389/fimmu.2024.1484373.

Wang, W., Yin, J., Ma, X., Zhao, F., Siedlak, S.L., Wang, Z., et al., 2017. Inhibition of mitochondrial fragmentation protects against Alzheimer's disease in rodent model. Hum. Mol. Genet. 26, 4118–4131. https://doi.org/10.1093/hmg/ddx299.

Wang, W., Zhao, F., Ma, X., Perry, G., Zhu, X., 2020. Mitochondria dysfunction in the pathogenesis of Alzheimer's disease: recent advances. Mol. Neurodegener. 15 (1), 30. https://doi.org/10.1186/s13024-020-00376-6.

Wang, X., Su, B., Siedlak, S.L., Moreira, P.I., Fujioka, H., Wang, Y., et al., 2008. Amyloid-β overproduction causes abnormal mitochondrial dynamics via differential modulation of mitochondrial fission/fusion proteins. Proc. Natl. Acad. Sci. USA 105 (49), 19318–19323. https://doi.org/10.1073/pnas.0804871105.

Wang, X., Wang, W., Li, L., Perry, G., Lee, H.G., Zhu, X., 2014. Oxidative stress and mitochondrial dysfunction in Alzheimer's disease. Biochim. Biophys. Acta Mol. Basis Dis. 1842, 1240–1247. https://doi.org/10.1016/j.bbadis.2013.10.015.

Wasilewski, D., Villalba-Moreno, N.D., Stange, I., Glatzel, M., Sepulveda-Falla, D., Krasemann, S., et al., 2022. Reactive astrocytes contribute to Alzheimer's disease-related neurotoxicity and synaptotoxicity in a neuron-astrocyte co-culture assay. Front. Cell Neurosci. 15, 739411. https://doi.org/10.3389/fncel.2021.739411.

Wilson, E.N., Do Carmo, S., Iulita, M.F., Hall, H., Austin, G.L., Jia, D.T., et al., 2018. Microdose lithium NP03 diminishes pre-plaque oxidative damage and neuroinflammation in a rat model of Alzheimer's-like amyloidosis. Curr. Alzheimer Res. 15, 1220–1230. https://doi.org/10.2174/1567205015666180904154446.

Xie, C., Aman, Y., Adriaanse, B.A., Cader, M.Z., Plun-Favreau, H., Xiao, J., et al., 2020. Culprit or bystander: defective mitophagy in Alzheimer's disease. Front. Cell Dev. Biol. 7, 391. https://doi.org/10.3389/fcell.2019.00391.

Xie, H., Guan, J., Borrelli, L.A., Xu, J., Serrano-Pozo, A., Bacskai, B.J., 2013. Mitochondrial alterations near amyloid plaques in an Alzheimer's disease mouse model. J. Neurosci. 33 (43), 17042–17051. https://doi.org/10.1523/JNEUROSCI.1836-13.2013.

Zhang, Y., Chen, H., Li, R., Sterling, K., Song, W., 2023. Amyloid β-based therapy for Alzheimer's disease: challenges, successes and future. Signal Transduct. Target Ther. 8, 248. https://doi.org/10.1038/s41392-023-01484-7.